Impact of Wi-Fi deployments and imperfect knowledge of Radar systems on Radar Wi-Fi coexistence

Anish Ashok

A dissertation
submitted in partial fulfillment of the
requirements for the degree of

Master of Science in Electrical Engineering

University of Washington

2017

Reading Committee:

Sumit Roy, Chair

James A. Ritcey

Program Authorized to Offer Degree:
Electrical Engineering

University of Washington

Abstract

Impact of Wi-Fi deployments and imperfect knowledge of
Radar systems on Radar Wi-Fi coexistence

Anish Ashok

Chair of the Supervisory Committee:
Professor Sumit Roy
Electrical Engineering

Spectrum sharing between dis-similar wireless communication systems has been a focus of on-going research to provide potential solutions for the lack of spectrum availability in the current usable range. This arises from the growing usage in mobile service applications that require very high data rates. In this thesis, we examine the coexistence between wireless local area networks (WLAN) and Radars. A large amount of licensed spectrum is allocated for the use of Radars [1] which allows for sufficient re-use of spectrum due to the spatially and temporally sporadic nature of Radar operation. We present the determination of *protection regions* around Radar primary users so that the aggregate interference from active Wi-Fi secondary users is kept within acceptable limits. The impact of Wi-Fi deployments - modelled as suitable random processes on the statistics of the protection region is studied. Using the Wi-Fi users, the location and mainbeam direction of the Radar is predicted. Also, a sophisticated software program to compute protection regions in the US is described.

[1] In the US, over 1700 MHz spectrum in the 225 MHz - 3.7 GHz range is allocated for Radar operations.

TABLE OF CONTENTS

LIST OF FIGURES

GLOSSARY

AP: Access Point

ATC: Air Traffic Control

CA: Collision Avoidance

CDF: Cumulative Distribution Function

CW: Contention Window

CSMA: Carrier Sense Multiple Access

DCF: Distributed Coordination Functions

DFS: Dynamic Frequency Selection

DOD: Department of Defense

FCC: Federal Communications Commission

FDR: Frequency Dependent Rejection

INR: Interference-to-Noise Ratio

ISM: Industrial, Scientific, Medical band

ITU: International Telecommunication Union

MAC: Medium Access Control

PDF: Probability Density Function

NTIA: National Telecommunications and Information Administration

OFDM: Orthogonal Frequency Division Multiplexing

PPP: Poisson Point Process

QPSK: Quadrature Phase Shift Keying

RMSE: Minimum Mean Squared Error

SINR: Signal-to-Interference-plus-Noise Ratio

SNR: Signal-to-Noise Ratio

TDMA: Time Division Multiple Access

U-NII: Unlicensed National Information Infrastructure

WLAN: Wireless Local Area Network

WI-FI: : WLAN based on the IEEE 802.11 Standard

ACKNOWLEDGMENTS

This work was supported in part under award AFRL CERFER FA8650-14-D-1722.

Thank you to my advisor, Professor Sumit Roy, for providing me with the guidance, patience and collaboration that enabled me to complete this stage of my academic career, without whom this would not be possible.

I would also like to thank Drs. Hossein Safavi, Farzad Hessar and Morteza Mehrnoush from the Fundamentals of Networking lab at the University of Washington for their ideas and helpful discussions.

Chapter 1

INTRODUCTION

The novelty of the proposed concepts center around spectrum sharing between dis-similar systems, i.e. with designated primary users sharing the frequency bands with secondary networks, unlike sharing in the unlicensed bands. The first instance of such primary-secondary sharing was the unlicensed reuse of local TV spectrum pursuant to the *TV White Spaces* ruling by the FCC in 2008 [1]. Pursuant to a Presidential directive [5], the FCC has undertaken that 150 MHz of spectrum between 3550-3700 MHz be made available for wireless broadband applications for Citizens Band Radio Service [6]. A comprehensive listing of U.S. Federal spectrum allocation for various radars is shown in Table 1.1. This is not, however, the first instance of spectrum sharing between a (licensed) radar and an unlicensed network. The globally unlicensed bands according to Article 5 of the ITU regulations are shown in Table 1.2. Wi-Fi operation in the 5 GHz (U-NII unlicensed bands in North America but not elsewhere) are already subject to Dynamic Frequency Select (DFS) requirements (requiring channel sensing and avoidance) to avoid interfering with various radars operational worldwide [10], [11]. Currently, only 36% of 5 GHz channels are unencumbered by radar protection requirements.

The potential of Radar-LTE coexistence in the 2700-2900 MHz bands was studied in [2] for different LTE deployment scenarios. However, for multiple secondary users it is assumed that the distance to the Radar is equal which is not practical. There have been some DoD studies [3], [4] in the US for Radars in 2700-2900 MHz bands. Protection for the Radar is determined by experimental measurements of interference from continuous wave, CDMA-QPSK and TDMA-QPSK waveform emissions.

Recent Radar coexistence studies with LTE and Wi-Fi using lab tests and field tests have

Table 1.1: NTIA Federal Spectrum Requirement Forecast for Radar Bands

Frequency band	Federal Government use
92–100 GHz	Airborne fire-control, beacons, atmospheric research, cloud detection, and synthetic vision radars
31.8–36 GHz	Airborne navigational, mapping, weather, beacon, terrain following and avoidance; aircraft carrier PAR, test range, atmospheric and oceanic research, altimeter, scatterometer, and synthetic vision radars
24.05–24.65 GHz	Doppler radiolocation, vehicle speed detection, scatterometer, and precipitation radars
15.4–17.3 GHz	Airborne and shipborne multimode search, battlefield, aircraft carrier PAR, fire-control, test range, ASDE, scatterometer, precipitation, atmospheric research, and spaceborne radars
13.25–14.2 GHz	Airborne and shipborne search and acquisition Doppler, airborne weather, altimeters, scatterometer, precipitation, environmental research, and spaceborne radars
8.5–10.55 GHz	Airborne and shipborne surveillance and navigation, fire-control, battlefield, maritime, weather, test range, airborne radionavigation, ATC, SAR's, altimeters, ASDE, scatterometer, vehicle speed detection, and spaceborne radars
5250–5925 MHz	NOAA weather radars, FAA TDWR, surveillance and air defense (airborne, shipborne, land-based), fire-control, maritime, test range, SAR's, altimeters, scatterometer, airborne, and spaceborne radars
4200–4400 MHz	Aircraft radar altimeters
3100–3650 MHz	DOD surveillance and air defense (airborne, shipborne, land-based), ATC, SAR's, altimeters, test range, and spaceborne radars
2700–3100 MHz	ATC, maritime, and weather radars; DOD shipborne, airborne, ground air surveillance radars; range control, and spaceborne radars
2310–2385 MHz	Planetary and lunar radar
1215–1390 MHz	ATC, SAR's, and DOD early warning air defense, battlefield, shipborne long-range surveillance, and spaceborne radars
890–942 MHz	Navy shipborne long-range surveillance, test range, NASA research, and wind profiler radars
420–450 MHz	DOD early warning and long-range surveillance radars; and wind profiler radars
216–220 MHz	DOD space surveillance radar
3–30 MHz	DOD OTH and surface wave radar

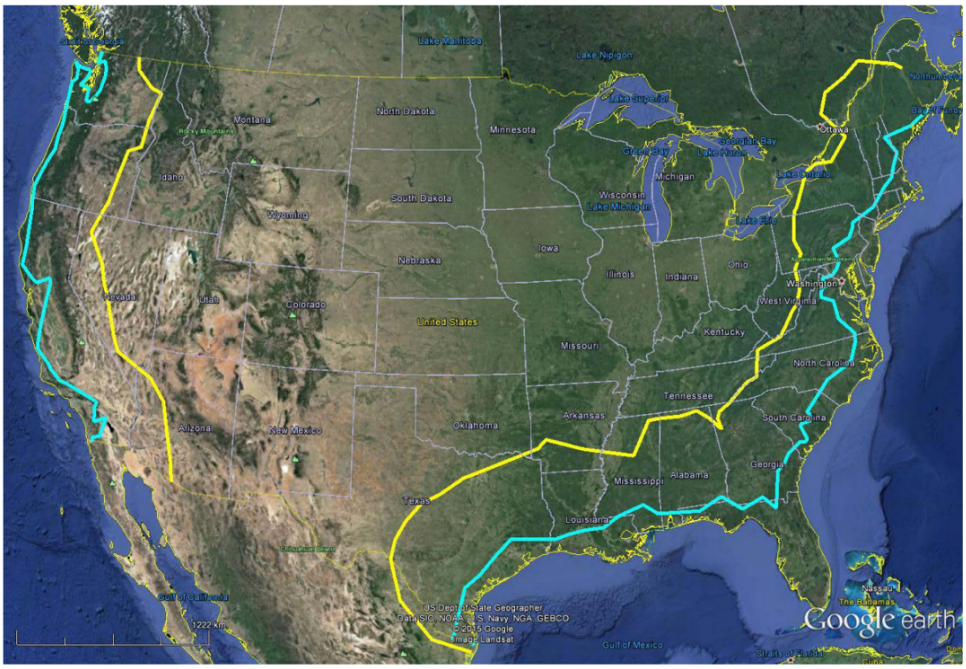

Figure 1.1: The original protection regions computed by the NTIA (outer yellow) were revised recently in [18] (inner blue). Even the revised region encompasses many population centers such as San Francisco and New York.

been performed for the SPN-43 Radar in the 3500-3700 MHz bands [14]. The distance to the Radar was assumed constant in all the experiments. The exclusion zones are determined using dedicated sensors to protect the Radar system. It is concluded that fixed protection regions by the FCC are unnecessary but it lacks the characterization of the interference at the Radar. The Radar Wi-Fi coexistence scenario must consider two important factors:

1. The impact of interference from Radar systems on the performance of WLANs, and

2. Measures needed to protect Radars from unlicensed wireless users.

In this work, we focus exclusively on the second factor; this is typically done by enforcing a *protection region* that represents a spatial domain surrounding the protected Radar location

in which co-channel transmission by WLAN users is forbidden[1]. We assume all radars are mono-static and the protection regions are determined by regulatory policy-making as a collaboration between NTIA and FCC, representing the need to balance incumbent protection and the needs of secondary civilian networks to set up an effective service [12]. Often, these protection regions can extend for hundreds of kilometers from the radar location, which if located near population centers, makes deployment of secondary systems inefficient. The NTIA in its initial Fast Track report [13], initially inferred that large geographical separation and frequency offsets were required to minimize interference from higher power macro cell networks to federal radar systems in the 3.5 GHz band. However, this analysis was later revised as the initial assumptions were significantly conservative (for example, 4G and beyond networks use smaller cells with lower power Base Stations) as shown in Figure 1.1. The above example and our own subsequent analysis emphasizes this important underlying point - that the determination of protection regions is significantly impacted by a multiplicity of factors on both the secondary (notably, the transmit power, deployment geometry, transmit antenna patterns) and primary (receiver sensitivity and operational margins, receive antenna patterns) side as well as the channel characteristics (distance and frequency dependant path loss, and any statistical effects such as small-scale fading and large-scale shadowing).

[1]Outside such regions, WLAN operation is allowed as it is deemed to offer only acceptable interference to primary receivers.

Table 1.2: Unlicensed bands per Article 5 of ITU regulations (Primary allocation in capital, secondary allocation in small letters)
Region 1: Europe, Africa, the former Soviet Union, Mongolia, and the Middle East west of the Persian Gulf.
Region 2: Americas including Greenland, and some of the eastern Pacific Islands.

Frequency range	Availability	Licensed users
6.765-6.795 MHz	Subject to local acceptance	FIXED SERVICE and Mobile service
13.553-13.567 MHz	Worldwide	FIXED and Mobile services except Aeronautical mobile (R) service
26.957-27.283 MHz	Worldwide	FIXED and MOBILE SERVICE except Aeronautical mobile service, CB Radio
40.66-40.7 MHz	Worldwide	Fixed, Mobile services and Earth exploration-satellite service
433.05-434.79 MHz	only in region 1, subject to local acceptance	AMATEUR SERVICE and RADIOLOCATION SERVICE
902-928 MHz	Region 2 only	FIXED, Mobile except aeronautical mobile and Radiolocation service
2.4-2.5 GHz	Worldwide	FIXED, MOBILE, RADIOLOCATION, Amateur and Amateur-satellite service
5.725-5.875 GHz	Worldwide	FIXED-SATELLITE, RADIOLOCATION, MOBILE, Amateur and Amateur-satellite service
24-24.25 GHz	Worldwide	AMATEUR, AMATEUR-SATELLITE, RADIOLOCATION and Earth exploration-satellite service (active)
61-61.5 GHz	Subject to local acceptance	FIXED, INTER-SATELLITE, MOBILE and RADIOLOCATION SERVICE
122-123 GHz	Subject to local acceptance	EARTH EXPLORATION-SATELLITE, FIXED, INTER-SATELLITE, MOBILE, SPACE RESEARCH (passive) and Amateur service
244-246 GHz	Subject to local acceptance	RADIOLOCATION, RADIO ASTRONOMY, Amateur and Amateur-satellite service

Chapter 2

COMPUTATIONS FOR VARIOUS WI-FI DEPLOYMENTS

2.1 Introduction

In this thesis, the role of the distribution of secondary users in determining the protection region for a Radar source is discussed. From [1] we know that the protection region for a Radar is a function of the time-spatial density. This does not give us information about the change in the protection region due to the density of secondary users. If one assumes that the time-spatial density increases linearly with the density of secondary users, then the aggregate interference and the protection region is an overestimate of the true values. Therefore, the relationship between the time-spatial density and the density of Wi-Fi networks is found using the analysis of the distributed coordination function discussed in [2]. Specifically, the role of the number of users associated with co-channel access points is investigated. By considering a Poisson point process (PPP) for the distribution of Wi-Fi APs, the results obtained in [2] allow us to characterize the change in the protection region as a function of the intensity of the PPP.

Section 2 uses the results obtained in [2] and Section 3 characterizes the Wi-Fi network distribution and the aggregate interference at a radar source.

2.2 Search Radar: Noise limited operation

Consider a rotating search radar limited where all interfering (Wi-Fi) sources lie in the same plane as the radar, and the desired target is at an elevation[1]. The performance characteristics

[1]Hence, in the sequel, consider a general radar antenna pattern $G(\theta, \phi)$ where these represent the azimuth and elevation angles, respectively; all interference calculations use the horizontal antenna pattern corresponding to $(\phi = 0)$ plane.

for the purely noise limited radar operation case is quantified in terms of the (desired) probability of detection P_D and acceptable false alarm rate P_{FA}. In turn, this determines the minimum SNR requirements at the radar receiver input (corresponding to a maximum operating range) and sets the baseline for comparison with any spectrum sharing regime. In order to enable cognitive reuse by secondary transmitters outside the protection region, we need to define rules for 'acceptable' interference at the radar. A recent DARPA program [7] suggested that a drop of 5% in P_D for fixed P_{FA} at the edge of radar operating range as being acceptable, which we adopt. This margin can be allocated to aggregate interference produced by a (random) spatial distribution of multiple Wi-Fi networks that are operational outside of the protection region.

At the monostatic radar receiver, the power of the reflected signal from the target, assuming free space propagation is given by the *Radar Equation* [15]:

$$P_R = \frac{P_T G^2 \lambda^2}{(4\pi)^3 d^4} \sigma \tag{2.1}$$

where the radar's instantaneous transmit power is P_T, G is the radar's antenna gain on both transmit and receive in the direction of the target, λ is the wavelength and d the distance from source to the target of interest, and σ represents the target's *radar cross section*.
Using the above, the effective SNR (SNR_{eff}) for reliable operation can be computed for a given probability of detection P_D and probability of false alarm P_{FA}. The minimum required SNR per pulse (SNR_{min}) is determined by the nature of any pulse integration employed in the detection chain, namely *coherent* and *non-coherent*. Using SNR_{min}, we can find the maximum interference level that can be tolerated by the radar, which we denote by $I_{\max}$. In turn, this determines the minimum separation between the radar and secondary users.

2.2.1 Noise-limited Radar Operation: Design Equations

For a radar transmitting a pulse train $x(t) = \sum_n \sqrt{P_T} s(t - \frac{n}{f_R})$ with pulse repetition frequency of f_R, the power of reflected signal from the target at the radar receiver is given by (2.1).

For a single received pulse, the signal-to-noise ratio (SNR) at the receiver input is

$$\mathrm{SNR}_p = \frac{P_T G^2 \lambda^2}{(4\pi)^3 d^4 N_0 f_{BW}} \sigma \tag{2.2}$$

with f_{BW} representing the pulse bandwidth and N_0 being the one-sided noise spectral density,

$$N_0 = FKT_E \tag{2.3}$$

where F is the receiver noise figure and T_E is the ambient temperature. Radar detection typically operates based on processing of multiple pulses received from the target. For a *coherent* receiver that integrates a number of pulses M reflected from the target, the resulting SNR at the detector input is increased by a factor of M, i.e.,

$$\mathrm{SNR}_{\mathrm{eff}} = M \frac{P_T G^2 \lambda^2}{(4\pi)^3 d^4 N_0 f_{BW}} \sigma \tag{2.4}$$

where $M = T_I \ f_R$, product of illumination time T_I and pulse repetition frequency f_R. The target illumination time T_I depends on radar scan rate as well as antenna pattern. Let θ_V and θ_H (in radian) denote the vertical and horizontal antenna beam width, respectively, then the antenna gain can be approximated as

$$G \approx \frac{4\pi}{\theta_H \theta_V} \rho_A \tag{2.5}$$

where ρ_A is the antenna efficiency, i.e., the radar concentrates the emitted power into an area of $\theta_V \theta_H$ with efficiency of ρ_A where the latter is typically 0.5. If the radar scans an area of Ω (steradians) (full search of azimuth/elevation implies $\Omega = 4\pi$) within a scan time of T_S, the illumination time is determined as:

$$T_I \approx T_S \frac{\theta_H \theta_V}{\Omega} \approx T_S \frac{4\pi \rho_A}{\Omega G} \tag{2.6}$$

Using (2.4)-(2.6) yields

$$\mathrm{SNR}_{\mathrm{eff}} = \frac{T_S}{\Omega} \frac{P_T G \lambda^2 f_R}{(4\pi)^2 d^4 N_0 f_{BW} L} \sigma \tag{2.7}$$

Note that the antenna efficiency ρ_A has been replaced by equivalent L that represents total losses in the system (e.g. transmission lines mismatch, loss of perfect coherence in pulse detector etc.).

The relationship between P_D, P_{FA} and SNR_p for a single pulse is fairly accurately expressed via the following equation [16]:

$$\mathrm{SNR}_p = \ln\left(\frac{0.62}{P_{FA}}\right) + 0.12\ln\left(\frac{0.62}{P_{FA}}\right)\ln\left(\frac{P_D}{1-P_D}\right) + 1.7\ln\left(\frac{P_D}{1-P_D}\right) \tag{2.8}$$

For a coherent receiver integrating M pulses, the SNR-performance relationship described in (2.8) with SNR_p should be replaced with the effective SNR at the detector input ($\mathrm{SNR}_{\mathrm{eff}}$), given by (2.7). Overall, the baseline performance of a noise-limited radar can be evaluated in two ways:

- Assuming that maximum operational range of the radar is known, calculate SNR from (2.2) or (2.7) for the maximum distance d. Then, using (2.8), we can trade-off between P_D and P_{FA}.

- Assuming that target P_D and P_{FA} are specified, estimate required SNR from (2.8) and then determine maximum range from (2.2) or (2.7).

As discussed subsequently, the interference from a Wi-Fi transmitter can be modelled as a Gaussian process, which is additive to the (thermal) AWGN noise. Thus radar system performance in the presence of (Wi-Fi) interference is determined by Signal-to-Interference-plus-Noise ratio (SINR) at receiver input. Using (2.7), this is given by

$$\mathrm{SINR} = \frac{T_S}{\Omega}\frac{P_T G\lambda^2 f_R}{(4\pi)^2 d^4 L\,(N_0 f_{BW} + I_{aggr})}\sigma \tag{2.9}$$

where I_{aggr} represents total interference power from secondary user(s). Therefore, maximum additional interference level $I_{\max}$ that can be tolerated is determined as follows:

$$\begin{aligned}\mathrm{SINR}_{\min} &\le \frac{T_S}{\Omega}\frac{P_T G\lambda^2 f_R\sigma}{(4\pi)^2 d^4 L\,(N_0 f_{BW} + I_{aggr})} \\ I_{aggr} &\le \frac{T_S}{\Omega}\frac{P_T G\lambda^2 f_R\sigma}{(4\pi)^2 d^4 L\,\mathrm{SINR}_{\min}} - N_0 f_{BW} = I_{\max}\end{aligned} \tag{2.10}$$

For a given deployment of Wi-Fi networks, the resulting aggregate interference at the radar receiver input I_{aggr} is modelled (statistically) in detail in Sec. 4. The difference between the received interference from secondary users (I_{aggr}) and the maximum tolerable interference at the radar receiver ($I_{\max}$) denotes the available margin (a positive margin implies secondary operation is possible).

For a single Wi-Fi AP, the interference power at the radar is given by

$$I_{SU \to Radar} = \frac{P_{SU} G(\theta)}{L_{Rd-SU}(d_{Rd-SU}) \mathrm{FDR}(\Delta f)} \tag{2.11}$$

where $L_{Rd-SU}(.)$ is the path-loss between radar and secondary user (SU) as a function of distance and $G(\theta)$ defines radar's antenna gain in the direction of SU (function of azimuth angle). $\mathrm{FDR}(\Delta f)$ is *frequency dependent rejection* factor that accounts for the mismatch between the spectral support of the transmitted signal and receiver input band; depending on spectral shape of transmitted signal $P(f)$ and receiver input filter $H(f)$, this is computed as

$$\mathrm{FDR}(\Delta f) = \frac{\int_0^\infty P(f) df}{\int_0^\infty P(f) H(f + \Delta f) df} \tag{2.12}$$

Since Wi-Fi and Radar are assumed to be spectrally flat and overlapping, the FDR is calculated as the ratio of corresponding bandwidths $FDR = \frac{20\mathrm{MHz}}{653\mathrm{KHz}} = 30.6$ [3]. Note that we have used IF 3-dB bandwidth for radar's receiver which is significantly smaller than RF 3-dB bandwidth of 10 MHz, since radar signal detection happens at IF.

2.3 Cumulative interference to Radar from randomly deployed Wi-Fi APs

Wi-Fi transmissions use OFDM signals, where each OFDM symbol is a linear combination of many randomly modulated sub-carriers. Hence, using central limit theorem, the transmitted OFDM signal in time-domain over the air is well-approximated as a Gaussian random process [8]. Thereafter, the transmitted signal undergoes linear time-invariant filtering - the equivalent of the channel and any receiver front-end processing such as the matched filter - that preserves the Gaussianity of the resulting interference process at the detector input

[17]. Thus, the power of any interference variance (I_{aggr}) at the detector input is additive to AWGN noise power, effectively raising the noise floor and system performance is determined by Signal-to-Interference-plus-Noise ratio (SINR) at the receiver input.

If multiple secondary users coexist with the radar simultaneously, the accumulated interference power at radar location can only be characterized statistically. The aggregate interference seen by the radar receiver is determined by several factors, notably the stochastic geometry of the deployment of the Wi-Fi networks (influences the distances and hence the component contributed to I_{aggr}) and the multiple access protocol employed (that determines which users are simultaneously active). Since users within a single Wi-Fi network share the common channel in time based on CSMA-CA, only (upto) *one* source can be active at any instant within one network. However, different Wi-Fi networks can simultaneously operate in the vicinity of a radar. In this work, we assume that each Wi-Fi network is simultaneously active (i.e. there is an active user), which represents a worst-case scenario and acts as upper bound on I_{aggr}, and focus exclusively on the impact of the geometry of Wi-Fi network deployment.

The stochastic geometry [21] of the Wi-Fi network deployments impact the aggregate interference at the radar receiver. Let the Wi-Fi APs and their associated users be randomly distributed in 2-D space according to a point process.

Without loss of generality, assume a radar located at the 2-D origin, with APs randomly distributed over Cartesian locations $\mathbf{x} \in R^2$. The aggregate interference from secondary users at the radar receiver is described as [20]:

$$I_{aggr} = \sum_{\mathbf{x}\in\Phi} \frac{P_{su} G(\theta_{\mathbf{x}})}{\mathrm{FDR}(\Delta f)} l(||\mathbf{x}||) \tag{2.13}$$

where P_{su} is the secondary user transmit power, $||\mathbf{x}||$ is the distance between radar and secondary access point, $l(.)$ describes the impulse response function that models signal attenuation (inverse of path loss) between the source and receiver, and $G(.)$ is radar's antenna gain in the azimuthal direction of interferer $\theta_{\mathbf{x}}$. Note that (2.13) is the aggregate interference from multiple Wi-Fi sources that are simultaneously active, and is the summation of

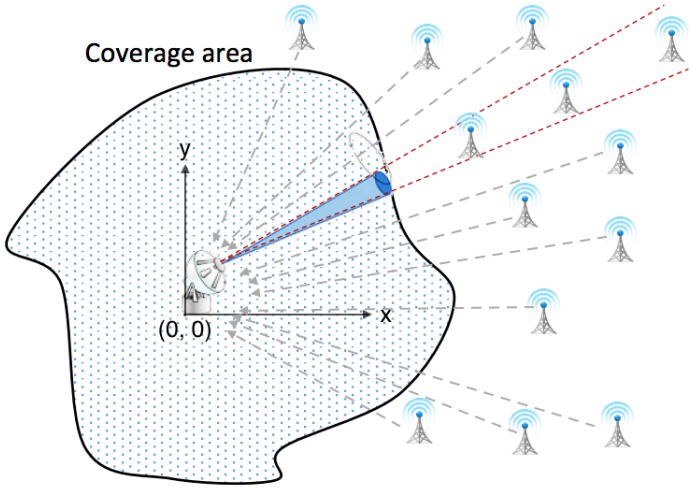

Figure 2.1: Aggregate interference from multiple Wi-Fi access points to radar receiver

components (2.11) that represent the interference from a single user. The random spatial deployment of Wi-Fi sources in turn implies the aggregate interference I_{aggr} at the radar must also be statistically characterized and plays an important role in performance analysis of radar detection under Wi-Fi interference. When Wi-Fi deployment may be modelled as a homogeneous Poisson point process with intensity λ, assuming propagation with pathloss exponent $\alpha = 4$ [2], it results in a Levy p.d.f for I_{aggr} [20]:

$$f_{I_{aggr}}(x) = \frac{\pi\lambda}{2x^{3/2}} exp\left(-\frac{\pi^3\lambda^2}{4x}\right) \tag{2.14}$$

It is worthwhile noting that the Levy p.d.f has a heavier tail than the Gaussian distribution and was derived [20] for the scenario of *no protection region* around the radar, i.e. nearby Wi-Fi sources contribute significantly to I_{aggr}.

[2] There exists no closed form solution other than $\alpha = 4$; the p.d.f for these must be obtained via numerical simulations.

2.3.1 Average and Variance of Aggregate Interference (μ_I, σ_I^2): Campbell's Theorem

Given the fact that the p.d.f of I_{aggr} is available in closed form for only a few specific cases, we now resort to the use of a basic result that allows characterization of the first and second moments of I_{aggr} for a broad class of spatial point processes. For a broad class of point processes with intensity function $\Lambda(\mathbf{x})$, the mean and variance of the random sum $\sum_{\mathbf{x}\in\Phi} f(\mathbf{x})$ is given by Campbell's theorem [20] as

$$E\left[\sum_{\mathbf{x}\in\Phi} f(\mathbf{x})\right] = \int_{\mathcal{R}^2} f(\mathbf{x})\Lambda(\mathbf{x})d\mathbf{x} \tag{2.15}$$

$$var\left[\sum_{\mathbf{x}\in\Phi} f(\mathbf{x})\right] = \int_{\mathcal{R}^2} f^2(\mathbf{x})\Lambda(\mathbf{x})d\mathbf{x} \tag{2.16}$$

Identifying $f(\mathbf{x}) = \frac{P_{su}G(\theta_{\mathbf{x}})}{FDR(\Delta f)}l(||\mathbf{x}||)$ from (2.13) allows us to compute the statistics of the aggregate interference at the radar input, as derived below.

Homogeneous Poisson Point Process (PPP)

We first consider the homogeneous PPP, for which $\Lambda(\mathbf{x}) = \lambda$. The average interference received at radar is calculated from (2.15) by integrating over the $\mathcal{R}^2$ plane, i.e.,

$$\mu_I = E[I_{aggr}] = \frac{\lambda P_{SU}}{\text{FDR}(\Delta f)} \int_{\mathcal{R}^2} G(\theta_x)l(||x||)dx \tag{2.17}$$

To incorporate the protection region, we assume there is a minimum separation distance between radar and active SUs, denoted as a function of azimuth angle θ, $d(\theta)$. Using polar coordinates and considering $l(r) = K_0 r^{-\alpha}$ for a general path loss model with radial symmetry, we obtain:

$$\begin{aligned}\mu_I &= \frac{\lambda P_{SU}K_0}{\text{FDR}(\Delta f)} \int_\theta \int_{d(\theta)}^{\infty} G(\theta)r^{1-\alpha}drd\theta = C_{\mu_I}\int_\theta G(\theta)d^{2-\alpha}(\theta)d\theta \\ C_{\mu_I} &= \frac{\lambda P_{SU}K_0}{\text{FDR}(\Delta f)(\alpha-2)}\end{aligned} \tag{2.18}$$

where $\alpha > 2$ is necessary to guarantee convergence of the integral over θ.

It is evident that the mean total interference is dependant on the choice of function $d(\theta)$

which in turn depends on the input radar antenna pattern $G(\theta)$. As we show in the next section, the choice of $d(\theta)$ can be optimized subject to some constraints.

The variance of aggregate interference - calculated from (2.16) - follows a similar approach to that for μ_I, resulting in:

$$\sigma_I^2 = \frac{\lambda P_{SU}^2 K_0^2}{\mathrm{FDR}^2(\Delta f)} \int_\theta \int_{d(\theta)}^\infty G^2(\theta) r^{-2\alpha} r dr d\theta = C_{\sigma_I^2} \int_\theta G^2(\theta) d^{2-2\alpha}(\theta) d\theta$$
$$C_{\sigma_I^2} = \frac{\lambda P_{SU}^2 K_0^2}{\mathrm{FDR}^2(\Delta f)(2\alpha - 2)} \tag{2.19}$$

where $\alpha > 1$ ensures convergence of the integration over r.

Non-homogeneous Poisson Process

We consider the Thomas cluster process, which belongs to the class of Neyman-Scott cluster processes[20] and is charterized by

$$\Lambda(\mathbf{x}) = \lambda_p \bar{c}$$

where λ_p is the intensity of a parent standard Poisson process that identifies a cluster head (AP); the number of (client) points associated with a cluster is independently Poisson distributed with density $\bar{c}$. Around every parent point, each daughter point is distributed according to a symmetric normal distribution in 2-D with variance ζ^2, i.e.,

$$f_{cl}(\mathbf{x}) = \frac{1}{2\pi\zeta^2} \exp(-\frac{||\mathbf{x}||^2}{2\zeta^2}) \tag{2.20}$$

where $\lambda = \lambda_p \bar{c}$, and $||\mathbf{x}||$ is the radial distance of the client with respect to cluster head (AP). The average interference is given by [20]

$$E[I_{aggr}] = E[I_{aggr-PPP(\lambda)}] + \frac{\bar{c} P_{su}}{FDR(\Delta f)(4\pi\zeta^2)} \int_{\mathcal{R}^2} G(\theta_{\mathbf{x}}) l(||\mathbf{x}||) \exp(-\frac{||\mathbf{x}||^2}{4\zeta^2}) d\mathbf{x} \tag{2.21}$$

where $E[I_{aggr-PPP(\lambda)}] = \mu_I$ is the average interference at the radar receiver when the Wi-Fi nodes are distributed according to a homogeneous PPP with density λ. The closed-form solution for the above integral is generally not available in closed form and must be computed numerically.

Note that the average interference at the radar is identical at each azimuth, when the Wi-Fi deployment follows a homogeneous PPP or the Thomas cluster process. We later will consider an inhomogeneous process in azimuth for the Wi-Fi deployment and explore it's impact on the aggregate interference via simulation.

2.4 Simulation Results for Omni Antenna Gain Pattern

For a radar receiver located at the origin, Wi-Fi nodes are scattered according to a PPP with density $\lambda = 10^{-6}$. The total area of deployment is a circle with outer radius of 20,000 km. In this section, we assume an omni-directional antenna pattern for radar with a gain of $G(\theta) = 10$ dBi. Secondary user power (including its antenna gain) is set to $P_{su} = 1.0$ watt, in line with commercial Wi-Fi devices. We consider a path-loss component of $\alpha = 4$ and outage probability of $P_{out,\max} = 0.1$. Aggregate interference power I_{aggr} at the radar receiver is simulated via the following steps:

i Initially, for a given omni-protection region ($d(\theta) = R$), the mean and variance of the I_{aggr} at the radar is calculated using Campbell's theorem.

ii For each $d(\theta)$, the numerically computed mean (μ_{theory}) and variance (σ^2_{theory}) based on Campbell's theorem are validated by Monte-Carlo simulations reported next. For every simulated case, a total of 1000 snapshots are generated and then sample mean/variance of aggregated interference is calculated.

2.4.1 Campbell's Theorem verification

The protection region in this case is circular, i.e. $d(\theta) = R$, where R is the radius of the protection region. Our simulation showed that sufficient number of snapshots must be generated to achieve reasonable accuracy. Figure 2.2 and 2.3 shows calculated mean and variance for a total of 1000 snapshots. It can be seen from the figures that Campbell's theorem is corroborated for a range of distances from 35 km up to 4500 km. The results are tabulated in Table 2.1.

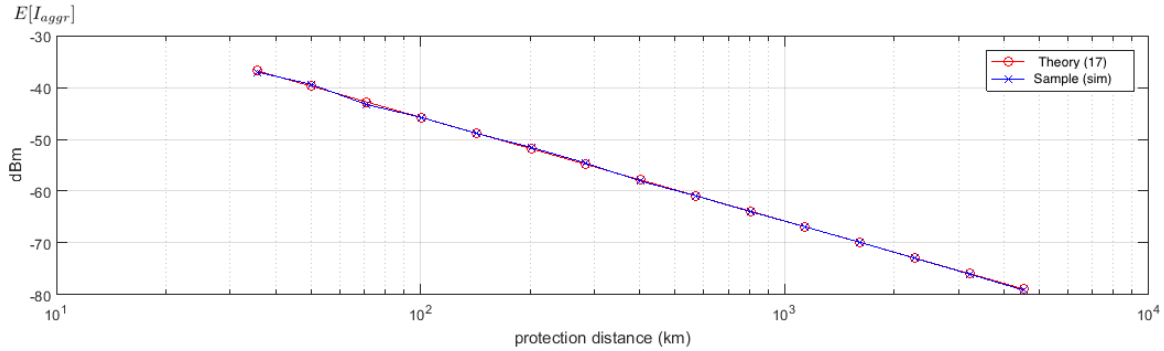

Figure 2.2: Mean of aggregate interference (1000 iterations)

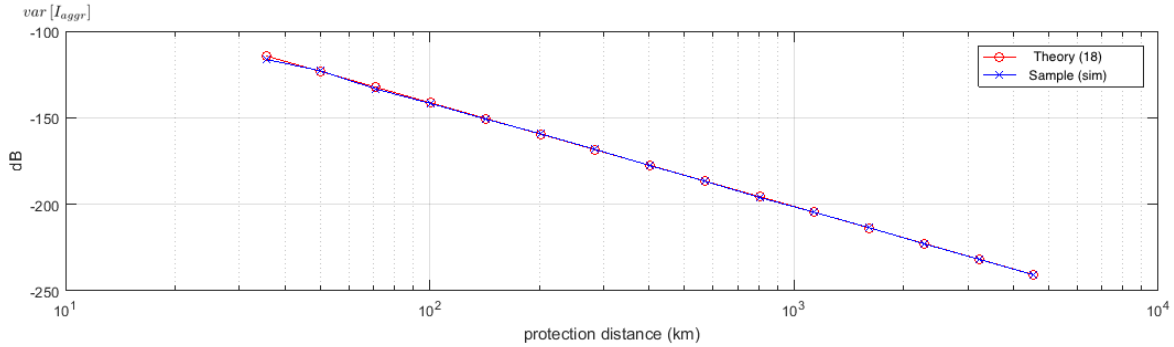

Figure 2.3: Variance of aggregate interference (1000 iterations)

2.4.2 Optimizing the protection region for homogenous PPP

In this section we explore the optimization of $d(\theta)$ subject to a constraint on I_{aggr} and outage probability, i.e.,

$$P(I_{aggr} > I_{\max}) \leq P_{out,\max}$$

where a typical value is $P_{out,\max} = 0.1$. We choose specific values of $I_{\max}$ (for example -50 dBm and -60 dBm) for which the protection region is optimized, i.e we find $d_{opt}(\theta)$ for which this constraint is satisfied, as described next. In following sections, we use three different methods for calculating $d(\theta)$, namely brute-force simulation, iterative Monte-Carlo and an

Table 2.1: Campbell's theorem verification table

$d(\theta) = R$ (km)	μ_{theory} (dBm)	$\mu_{sample-1000}$	σ^2_{theory} (dB)	$\sigma^2_{sample-1000}$	Time (s)
35.6	-36.7733	-37.0256	-114.3099	-116.2947	22.22
50.3	-39.7836	-39.4451	-123.3408	-122.9496	21.81
71.1	-42.7939	-43.2891	-132.3717	-133.4190	22.24
100.6	-45.8042	-45.8034	-141.4026	-141.7799	21.73
142.3	-48.8145	-48.8520	-150.4335	-150.7537	21.87
201.2	-51.8248	-51.5716	-159.4644	-159.2130	22.07
284.5	-54.8351	-54.6039	-168.4953	-168.2962	22.10
402.4	-57.8454	-58.0629	-177.5262	-177.6571	22.11
569.0	-60.8557	-60.8903	-186.5571	-186.6209	22.00
804.8	-63.8660	-63.9500	-195.5880	-196.1037	21.81
1138.1	-66.8763	-66.8855	-204.6189	-204.6284	21.79
1609.5	-69.8866	-69.8694	-213.6498	-213.5399	21.69
2276.2	-72.8969	-72.9489	-222.6807	-222.8702	21.70
3219.0	-75.9072	-76.0084	-231.7116	-231.7877	20.88
4552.4	-78.9175	-79.1378	-240.7425	-240.7864	20.40

analytical method based on Gaussian assumption.

Numerical brute-force algorithm for omni-protection region

For simulating the brute-force method, we utilize parameters in Section 2.4, with $I_{\max} = -50$ dBm. The steps described below are followed to calculate the optimal protection distance:

i Initially, pick $d(\theta) = 100$ km. For a given value of $d(\theta)$, a histogram of I_{aggr} is generated for 1000 snapshots.

ii Using the $I_{\max}$ value, the outage probability $P_{out} = P[I_{aggr} > I_{\max}]$ is calculated and compared against $P_{out,\max}$.
If $P_{out} \leq P_{out,\max}$, then stop; the current value of $d(\theta)$ is the optimum $d_{opt}(\theta)$.

iii If $P_{out} > P_{out,\max}$, then repeat experiment after incrementing $d(\theta)$ by $\Delta = 0.5$ km.

Figure 2.4 shows the variation of P_{out} vs. $d(\theta)$, from which we observe that P_{out} oscillates around its true value for averaging over 1000 snapshots. We then use a cubic spline function for smoothing with smoothing parameter of 0.001; and also tabulate the results in Table 2.2. The brute-force method takes extraordinary time for completion; in the next section, we utilize an iterative Monte-Carlo method that is significantly faster.

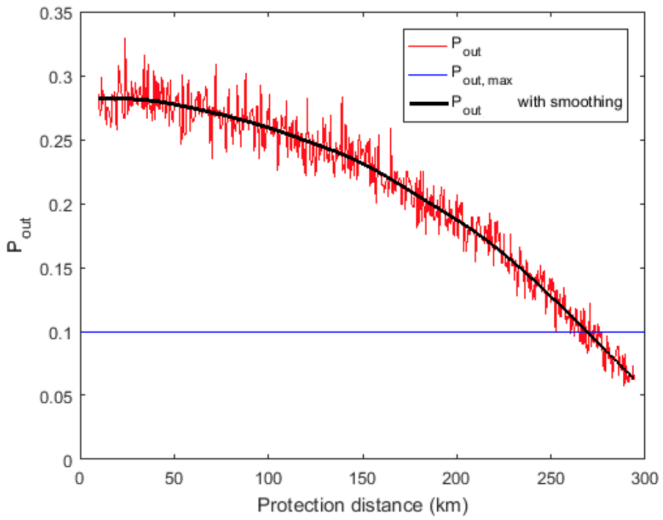

Figure 2.4: P_{out} vs. $d(\theta)$ - Numerical brute force algorithm ($I_{\max}$ = -50dBm)

Iterative Monte Carlo simulation to determine $d_{opt}(\theta)$

In this section, we adopt an adaptive on-line algorithm for updating the values of $d(\theta)$ based on the Adam algorithm proposed in [27]. Adaptive moment estimation (Adam) computes an adaptive learning rates for each parameter by using an exponentially decaying average of

Table 2.2: Effect of smoothing in Figure 2.4

	$d_{opt}(\theta)$ (km)	P_{out}	Time (s)
Without smoothing	252.5	0.100	4082.4
With smoothing	269.9	0.098	4082.4

past squared gradients (v_t) and the past gradients (m_t). The algorithm steps are outlined below:

i The gradient is chosen as $g_t = P_{out} - P_{out,max}$.

ii Initialize: Stepsize $\alpha = 100$, $\beta_1 = 0.9, \beta_2 = 0.999$ and $\epsilon = 10^{-8}$.

iii The first moment vector (m), second moment vector (v) and timestep vector (t) are initialized as
$m \leftarrow 0, v \leftarrow 0, t \leftarrow 0$ and $d(\theta) = 10$ km.

iv **while** $d(\theta)$ has not converged, **do**
$t \leftarrow t + 1$
run Monte Carlo experiment 1000 times to obtain P_{out-t}
$g_t \leftarrow P_{out-t} - P_{out,\max}$
$m_t \leftarrow \beta_1 m_{t-1} + (1 - \beta_1) g_t$
$v_t \leftarrow \beta_2 v_{t-1} + (1 - \beta_2) g_t^2$
$\alpha_t \leftarrow \alpha(1 - \beta_2^t)^{\frac{1}{2}}/(1 - \beta_1^t)$
$\hat{m}_t \leftarrow \beta_1 m_{t-1} + (1 - \beta_1) g_t$
$\hat{v}_t \leftarrow \beta_2 v_{t-1} + (1 - \beta_2) g_t^2$
$d(\theta)_t \leftarrow d(\theta)_{t-1} - \alpha_t \hat{m}_t/(\hat{v}_t)^{\frac{1}{2}} + \epsilon)$
end while

v stop: $d(\theta)_t$ is optimal protection distance

In order to check convergence at each iteration, a histogram of I_{aggr} is generated, using 1000 snapshot results for a given value of $d(\theta)$. Using $I_{\max}$ value, the outage probability ($P_{out} = P[I_{aggr} > I_{\max}]$) is calculated and compared against $P_{out,\max}$. If $|P_{out} - P_{out,\max}| \leq \delta = 0.005$, then algorithm stops; keeping current value of $d(\theta)$ as $d_{opt}(\theta)$. Figure 2.5 shows the updating process of $d(\theta)$ in time (seconds) from initialization to convergence. The benefits, in terms of time to convergence, of using the iterative update is captured in Table 5 which shows very significant gains.

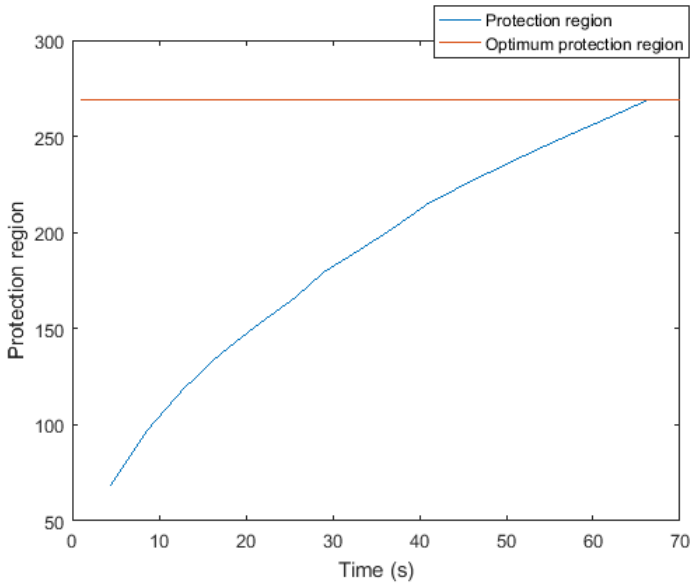

Figure 2.5: Update of $d(\theta)$ vs. Time (s) - Iterative Monte Carlo simulation ($I_{\max}$ = -50dBm)

Table 2.3: Comparison of processing time for finding d_{opt}

Algorithm	$d_{opt}(\theta)$ (km)	P_{out}	Time (s)
Numerical brute-force	269.9	0.100	4082.4
Iterative Monte Carlo	268.8	0.099	66.2

Gaussian assumption for distribution of I_{aggr}

In [9], the distribution of I_{aggr} was approximated as a normal distribution $N(\mu_I, \sigma_I^2)$, as it allows further inroads towards an analytical determination of the optimum protection region as summarized below. With the Gaussian assumption, the outage probability can be determined as

$$P_{outage} = \Pr\{I_{aggr} > I_{\max}\} = Q\left(\frac{I_{\max} - \mu_I}{\sigma_I}\right) \tag{2.22}$$

where $Q(.)$ function is the tail probability of the standard normal distribution. It is desired to set an upper bound for probability of outage, $P_{out,\max}$, i.e.,

$$\begin{aligned} &P_{outage} \leq P_{out,\max} \rightarrow Q\left(\frac{I_{\max} - \mu_I}{\sigma_I}\right) \leq P_{out,\max} \\ &I_{\max} \geq \mu_I + \sigma_I Q^{-1}\left(P_{out,\max}\right) \end{aligned} \tag{2.23}$$

Here, the coexistence criteria is defined by (3.4). This inequality is trivially achieved by letting $d(\theta) \rightarrow \infty$ (apparent from (2.18) for example). In order to avoid this, we *minimize the total protection area* subject to net interference limit as formulated in following optimization problem:

$$d_{opt} = \arg\min_{d(\theta)} \int_0^{2\pi} d^2(\theta) d\theta \tag{2.24}$$

subject to:

$$\mu_I + \sigma_I Q^{-1}\left(P_{out,\max}\right) \leq I_{\max} \tag{2.25}$$

For a general antenna pattern $G(\theta)$, it is proven in the appendix that optimum protection distance $d_{opt}(\theta)$ is proportional to $G^{1/\alpha}(\theta)$ with a constant γ that is determined by numerically solving following equation:

$$\begin{aligned} &d_{opt}(\theta) = \gamma G^{\frac{1}{\alpha}}(\theta) \qquad \text{where} \\ &\mathcal{A}\gamma^{2-\alpha} + \mathcal{B}\gamma^{1-\alpha} - I_{\max} = 0 \end{aligned} \tag{2.26}$$

in which $\mathcal{A}$ and $\mathcal{B}$ are determined by:

$$\mathcal{A} = C_{\mu_I} \int_0^{2\pi} G^{\frac{2}{\alpha}}(\theta) d\theta$$
$$\mathcal{B} = Q^{-1}\left(P_{out,\max}\right) \sqrt{C_{\sigma_I^2} \int_0^{2\pi} G^{\frac{2}{\alpha}}(\theta) d\theta} \tag{2.27}$$

2.4.2.0.1 Comparison of the Gaussian assumption with Monte Carlo Simulation:

In order to evaluate accuracy of Gaussian assumption, here we compare calculated protection distance with that of Monte-Carlo simulations. The maximum interference level $I_{\max}$ is varied from -70 dBm to -40 dBm to cover both large and small cases of protection distance. Table 2.4 compares resulting distances as well as simulated outage probability for both methods.

Table 2.4: Comparison of calculated protection distance and resulting outage probability for Gaussian versus Monte-Carlo

$I_{\max}(dBm)$	-40	-50	-60	-70
Iterative Monte-Carlo d_{opt} km (P_{out})	41.41 (0.098)	261.49 (0.102)	654.7 (0.100)	1787.5 (0.101)
Gaussian assumption d_{opt} km (P_{out})	112.08 (0.057)	262.45 (0.098)	659.0 (0.106)	1809.0 (0.089)

Monte-Carlo method achieves the desired outage probability of $P_{out} \approx 0.1$ for all cases of $I_{\max}$. For smaller values of $I_{\max}$, Gaussian assumption results in similar P_{out}, d_{opt}, providing an accurate analytical solution. For large values such as $I_{\max} = -40$ dBm, Gaussian assumption resulted in an outage probability of $P_{out} \approx 0.057$ that is significantly smaller than the allowed bound. Therefore, the corresponding protection distance is significantly larger than

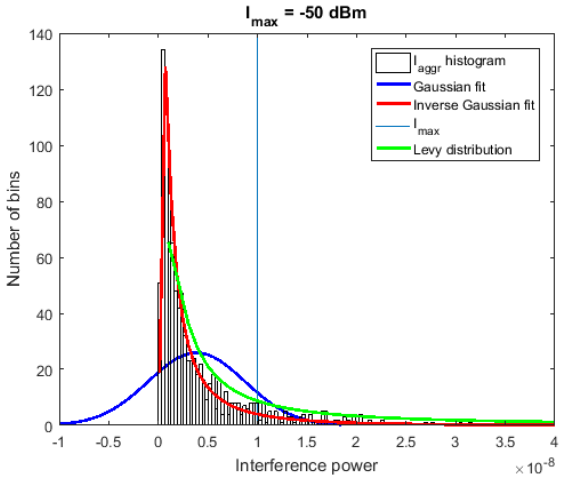

Figure 2.6: Gaussian fit is not a good approximation

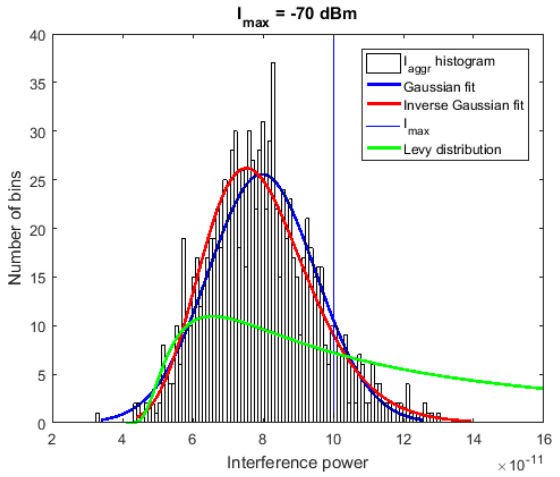

Figure 2.7: Gaussian fit is a reasonable approximation

Monte-Carlo method (112 km versus 41 km) [3].

In Figures 2.6 and 2.7, we plot the histogram of I_{aggr} obtained from the above simulation scenario (for two cases of $I_{\max} = -50, -70$ dBm), and compare with the Gaussian, Inverse Gaussian and Levy p.d.f. In [20], the Inverse Gaussian distribution is shown to be a better fit when compared to the Levy distribution in the case of active Wi-Fi nodes outside the protection region, with p.d.f given by (2.28).

$$f_I(x) = \left[\frac{\kappa}{2\pi x^3}\right]^{1/2} exp\left(-\frac{\kappa(x-\nu)^2}{2\nu^2 x}\right) \tag{2.28}$$

where $E[I] = \nu$ and $var(I) = \nu^3/\kappa$.

2.4.3 Poisson Cluster Process

In this and next sections, we consider Wi-Fi deployments that are *spatially inhomogeneous* point processes. Here, we have focused on Poisson Cluster Processes for spatial distribution

[3]The approximate value from Gaussian method in such cases can be used to initialize the iterative Monte-Carlo simulation, which will then find the accurate value quickly.

of nodes. A cluster process is created using a parent process of density λ_p that defines the location of the clusters; and a child process that is created around each cluster point. The number of points in a cluster is a Poisson random variable with a mean of $\bar{c}$. These points are scattered around the cluster center, with a Gaussian distribution of zero mean and variance of ζ.

Similar to previous results, we use a radar antenna pattern of $G(\theta) = 10$ dBi, along with $\lambda_p = 10^{-7}\,\mathrm{km}^{-2}$, $\bar{c} = 100$ and $\zeta = 800$ for the Poisson cluster (Thomas) process. Path-loss exponent is set to $\alpha = 4$, $I_{\max} = -60$ dBm and $P_{out,\max} = 0.1$ is utilized. The simulations are conducted for an area with outer radius of 20,000 km and 1000 snapshots are used for averaging. The protection distance is still a circle with radius $d_{opt}(\theta)$ and results from the fact that the spatial process, while inhomogeneous, exhibits radial symmetry of cluster/node locations (as in Figure 2.9) and all sources use omni-directional antenna pattern.

2.4.3.1 Campbell's theorem verification

Similar to Section 2.4.1, Campbell's theorem is verified numerically using new spatial distribution and for various protection distances. Figure 2.8, shows average interference measured at the radar receiver from Wi-Fi nodes with a Poisson cluster distribution. It presents a perfect match between what Campbell predicts for average interference, and our simulation results.

It is insightful to compare average interference from a Poisson cluster process with a corresponding homogeneous PPP. From (2.21), we know that the increase in average interference power, compared to the homogeneous PPP, is given by

$$\frac{\bar{c}P_{SU}}{FDR(\Delta f)(4\pi\zeta^2)}\int_{\mathcal{R}^2} G(\theta_{\mathbf{x}})l(||\mathbf{x}||)\exp(-\frac{||\mathbf{x}||^2}{4\zeta^2})d\mathbf{x}$$

This value tends to 0 for large values of protection regions, therefore the increase in interference power due to clustering is negligible. We have simulated a cluster process with $\lambda_p = 10^{-7}$ and $\bar{c} = 2000$, and for $\zeta \in (0, 300]$; no visible difference was observed compared to corresponding homogeneous PPP.

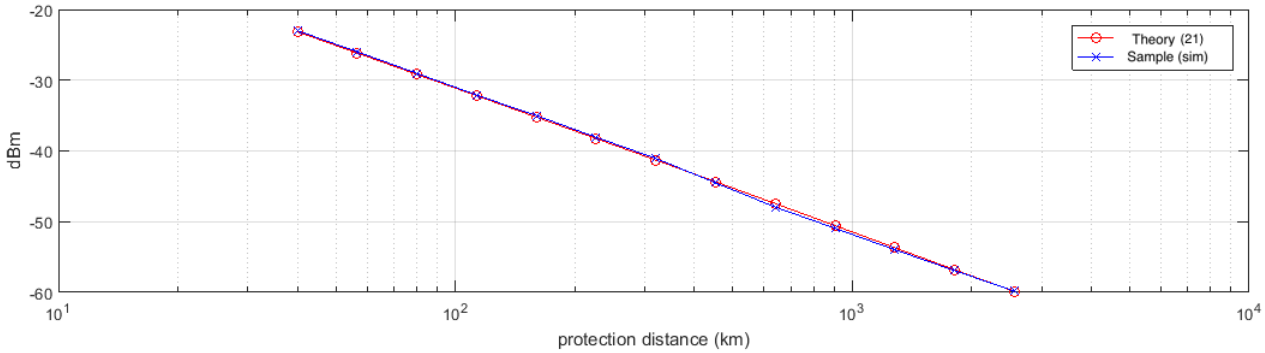

Figure 2.8: Mean of aggregate interference (1000 iterations)

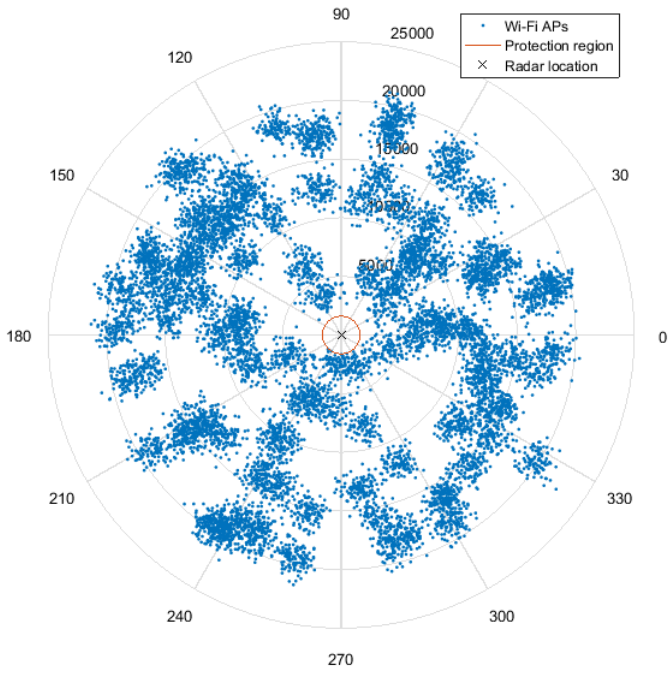

Figure 2.9: One realization of the Thomas cluster process

The optimum protection region can be found using the same methods described for the homogeneous PPP. A fair comparison of the Thomas cluster process with the homogeneous PPP is made by setting $\lambda = \lambda_p \bar{c}$. Table (2.5) shows optimum protection regions, using the iterative Monte Carlo simulation, for both cases of spatial distributions. The resulting

distances are very close, which is in line with our previous observation about average I_{aggr}.

Table 2.5: Comparison of protection distance ($I_{\max}$ = -60 dBm, $\lambda_p = 10^{-7}, \bar{c} = 10$)

Point process	Intensity	d_{opt}
Homogeneous PPP	$\lambda = \lambda_p \bar{c}$	662.8
Thomas cluster process	$\lambda_p, \bar{c}$	663.2

2.4.4 Inhomogeneous PPP

In this section, we explore an inhomogeneous PPP that is *not* symmetric in azimuth angle. From [21], initially a homogeneous PPP with intensity λ_0 is simulated. Then, points are randomly removed with a *spatially dependant* probability $1 - \frac{\lambda(\mathbf{x})}{\lambda_0}$. This is done by assigning every point with a random number uniformly distributed in $[0, 1]$. Let random number u_n be assigned to the n^{th} point. The point is deleted if $u_n < 1 - \frac{\lambda(\mathbf{x})}{\lambda_0}$. The resulting point process has an intensity $\lambda(\mathbf{x})$ and a realization is shown in Figure 2.10. The resulting density function $\lambda(x)$ of the point process is shown in Figure 2.11.

For such an inhomogeneous point process, the protection region is found for small sectors assuming a homogeneous PPP. For a given sector, Campbell's theorem is verified and a protection distance is obtained. This is repeated locally for all (sufficiently small) sectors to obtain the overall protection region. The result is shown in Figure 2.12 and compared with the protection region for a corresponding homogeneous PPP with intensity $\frac{\lambda_0}{2}$. In this case, the protection region is not circular. However, the total area of protected region for both cases is very similar, as shown in Table 2.6.

2.5 Simulation Results for typical Radar gain pattern

In this section, we investigate the case of realistic (non-omni) antenna gain patterns at the radar receiver, using the model in [19]. The maximum gain of the antenna (main lobe) is

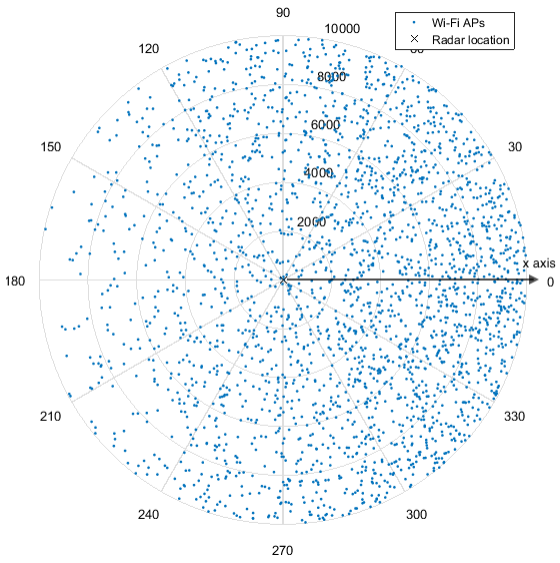

Figure 2.10: One realization of the inhomogeneous PPP

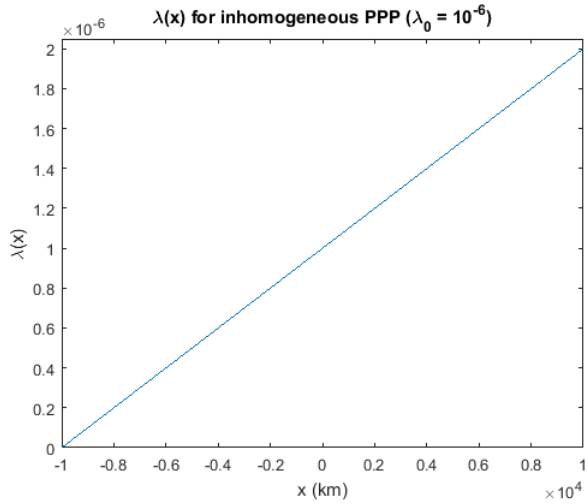

Figure 2.11: $\lambda(x)$

typically in the range of $22 < G_{\max} < 48$ dBi. The following piece-wise function describes

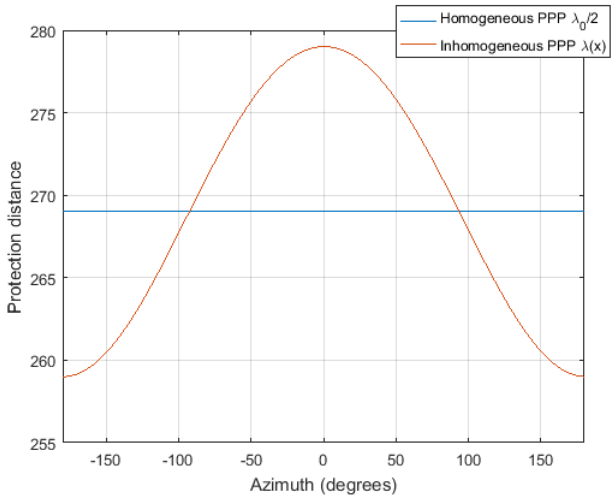

Figure 2.12: Protection region for the inhomogeneous PPP Wi-Fi deployment, compared with the homogeneous PPP Wi-Fi deployment ($\lambda_0 = 2\text{x}10^{-6}, I_{\max} = -50$ dBm)

Table 2.6: Fair comparison with a homogeneous PPP having $\frac{\lambda_0}{2}$ intensity for I_{max} = -50 dBm

Poisson Point Process	Intensity	Area of protection region (sq. km)
Inhomogeneous	$\lambda(x)$	2.2733x10^5
Homogeneous	$\frac{\lambda_0}{2}$	2.2770x10^5

antenna gain $G(\theta)$ versus azimuth angle:

$$G(\theta) = \begin{cases} G_{\max} - 0.0004 * 10^{G_{\max}/10}\theta^2 & \theta \in [0, \theta_M] \\ 0.75G_{\max} - 7 & \theta \in [\theta_M, \theta_R] \\ 53 - G_{\max}/2 - 25\log(\theta) & \theta \in [\theta_R, \theta_B] \\ 11 - G_{\max}/2 & \theta \in [\theta_B, 180] \end{cases} \tag{2.29}$$

where $\theta_M = 50\sqrt{0.25G_{\max} + 7}/10^{G_{\max}/20}$, $\theta_R = 250/10^{G_{\max}/20}$ and $\theta_B = 48$. Figure 2.13 shows antenna gain versus azimuth with a main lobe value of $G_{\max} = 33.5$ dBi.

Following the same approach as the previous sections, the results for the homogeneous PPP are used as a baseline for the non-omni gain pattern. It is important to note that the protection region is now *not* radially symmetric. It is larger along the main beam direction

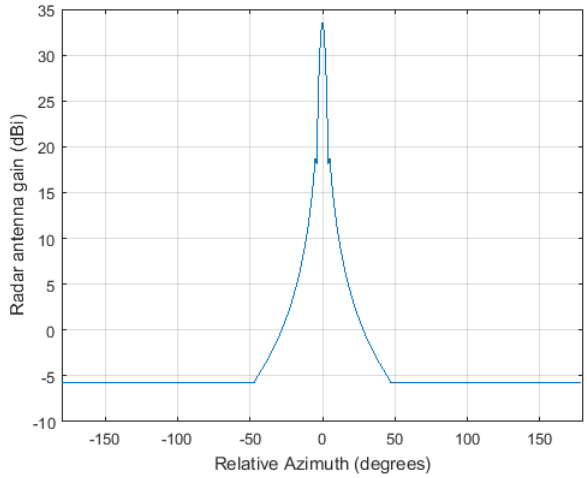

Figure 2.13: Radar antenna gain vs. Azimuth

of the radar, and significantly smaller in the other directions, as in Figure 2.14. Clustering in the deployment geometry by itself has little effect on the protection region (same as what was observed in Section 2.4.3) but inhomogeneous PPP models that are not radially symmetric does shift the protection region towards the denser portion of the Wi-Fi deployment, as is intuitively sensible.

2.5.1 Homogeneous PPP

We have calculated protection distance $d_{opt}(\theta)$, using antenna pattern provided in (2.29). Table 2.7 provides simulation results for different cases of $I_{\max}$. Comparing theoretical mean from Campbell (2.15) with sample averages verifies Campbell theorem for the case of directional antenna as well. In addition, Table 2.7 shows outage probability, minimum/maximum protection distance d_{opt} (corresponding to minimum/maximum $G(\theta)$) for both cases of Monte-Carlo simulation as well as Gaussian assumption method.

Figures 2.14 and 2.15 presents $d_{opt}(\theta)$ as a function of azimuth for two cases of $I_{\max} = -50, -70$ dBm. In each figure, Monte-Carlo results are compared with analytical results from Gaussian assumption. We can see that for $I_{\max} = -60, -70$dBm, both methods have

very similar outcomes and Gaussian assumption provides an accurate estimate of $d_{opt}(\theta)$. However, for $I_{\max} = -50$, Gaussian assumption leads to a more conservative protection region with larger distances and lower outage probability.

Table 2.7: Comparing d_{opt}, P_{out} for Monte-Carlo with Gaussian method

$I_{\max}$	-50 dBm	-60 dBm	-70 dBm
Iterative Monte-Carlo d_{opt} km (mainlobe) d_{opt} km (sidelobe) (P_{out})	509.14 53.16 (0.100)	2055 214.6 (0.103)	5173.1 540.1 (0.104)
Gaussian assumption d_{opt} km (mainlobe) d_{opt} km (sidelobe) (P_{out})	845.75 88.32 (0.057)	2023.9 211.31 (0.125)	5242.8 547.41 (0.098)
Theoretical mean (dBm) Equation (2.15)	-55.76	-63.33	-71.60
Sample mean (dBm)	-56.38	-63.26	-71.63

The conservative result from Gaussian assumption can also be understood from a different point of view, notably p.d.f. of I_{aggr}. Figure 2.16 and 2.17 shows histogram of I_{aggr} (calculated from simulation results) and compares that with Gaussian and Inverse-Gaussian p.d.f. (with same mean and variance). It is observed that Gaussian p.d.f mimics I_{aggr} histogram with very high accuracy, for the case of $I_{\max} = -70$ dBm. On the other hand, Gaussian p.d.f is a very poor approximation for the histogram in case of $I_{\max} = -50$ dBm. Inverse-Gaussian (2.28), however, presents a very accurate model for p.d.f. of I_{aggr} in both cases.

For smaller protection distances (where Gaussian is a poor model), the heavier tails in

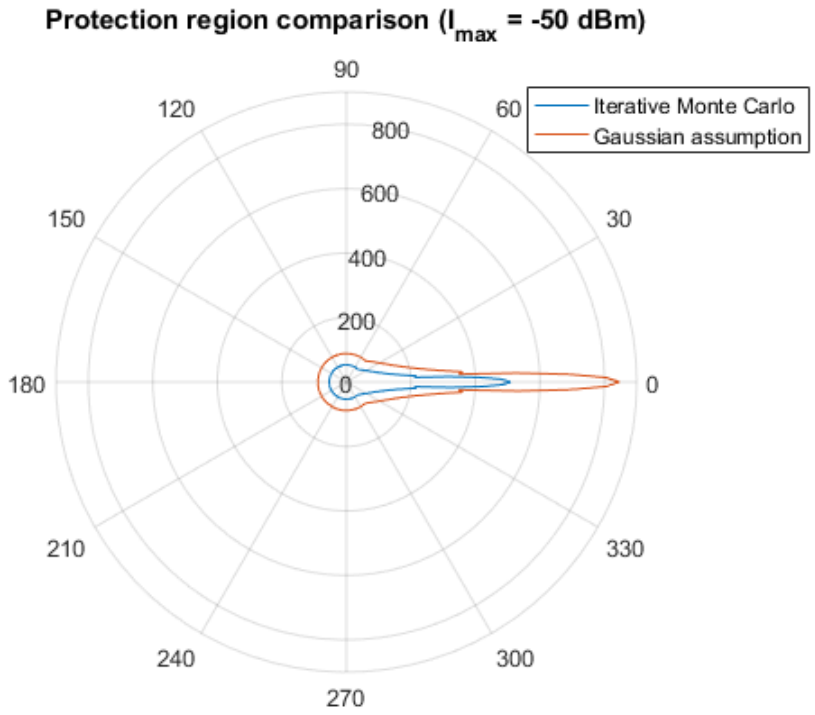

Figure 2.14: For $I_{\max}$ = -50 dBm, the Gaussian assumption is not a good approximation for distribution of I_{aggr}

the distribution of I_{aggr} arise from the contributions to the aggregate interference power from Wi-Fi users that are at/close to the boundary of the protection region, which are possibly orders of magnitudes larger than the far-off sources. As the protection region increases, the effect of the interference from Wi-Fi sources in the vicinity of the protection region (relative to the rest) reduces and the distribution becomes less heavy-tailed or more symmetric.

2.5.2 Inhomogeneous PPP

Following the approach in Section 2.4.4, the protection region for an inhomogeneous distribution of Wi-Fi nodes, and with a directional antenna pattern at radar, is calculated and plotted in Figure 2.18. The result is compared with the protection region of a homogeneous PPP with intensity $\frac{\lambda_0}{2}$. Intensity $\frac{\lambda_0}{2}$ is chosen so that the average number of Wi-Fi APs in both processes (homogeneous and inhomogeneous) are equal. The computed protection

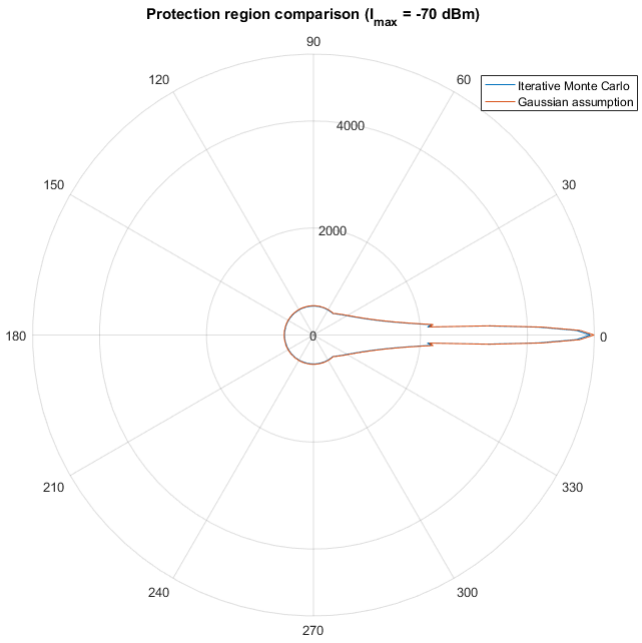

Figure 2.15: For $I_{\max}$ = -70 dBm, the Gaussian assumption is a good approximation for distribution of I_{aggr}

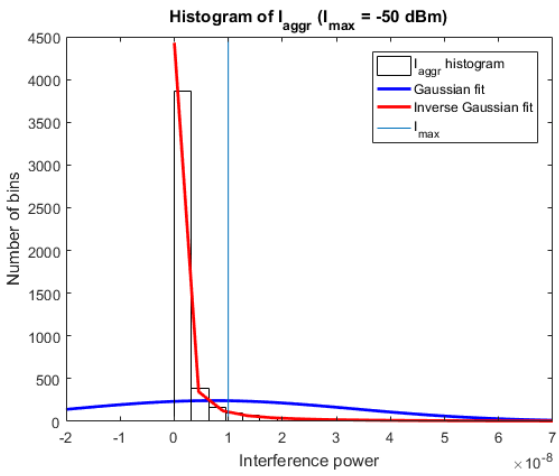

Figure 2.16: Gaussian fit is not a good approximation

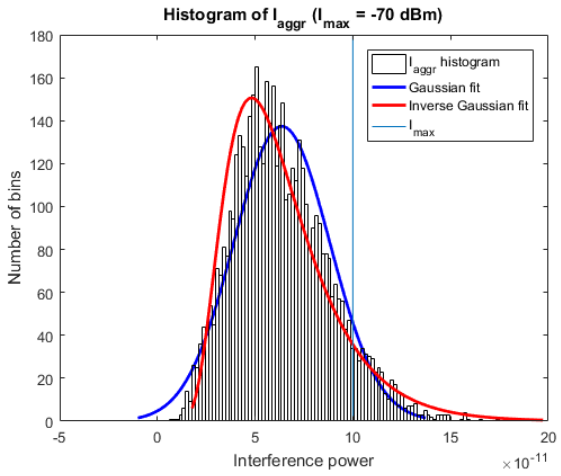

Figure 2.17: Gaussian fit is a reasonable approximation

region area for both cases is shown in Table 2.8.

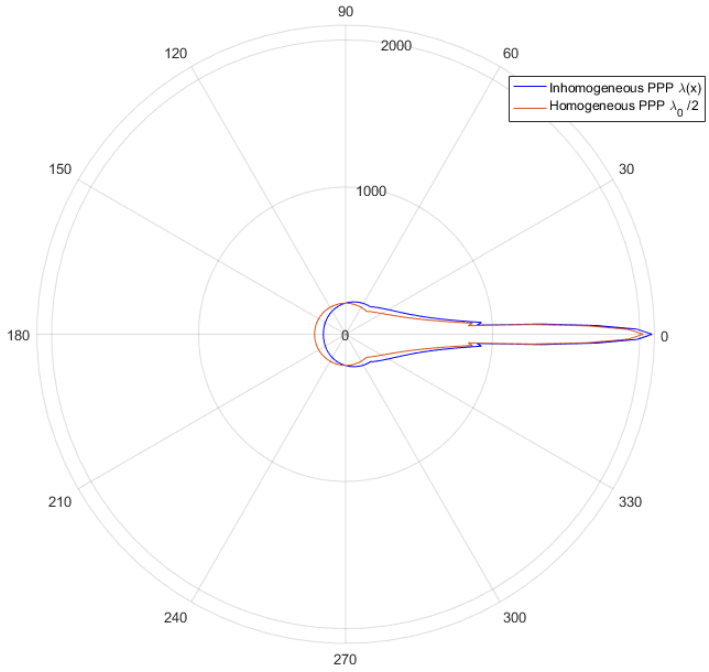

Figure 2.18: Protection region for the inhomogeneous PPP Wi-Fi deployment, compared with the homogeneous PPP Wi-Fi deployment ($\lambda_0 = 2\text{x}10^{-6}, I_{\max} = -60$ dBm)

Table 2.8: Fair comparison with a homogeneous PPP having $\frac{\lambda_0}{2}$ intensity

Poisson Point Process	Intensity	Area of protection region (sq. km)
Inhomogeneous	$\lambda(x)$	4.1664x10^5
Homogeneous	$\frac{\lambda_0}{2}$	4.1105x10^5

2.6 Statistics of optimal protection region

Due to the simulation model used and the stochastic nature of the Wi-Fi deployments, the statistics of the protection region need to be characterized.

2.6.1 Numerical Brute force

For simulating the brute-force method, we utilize parameters in Section 2.4, with $I_{\max} = -50$ dBm. The algorithm is shown below:

i Initially, pick $d(\theta) = 100$ km. For a given value of $d(\theta)$, a histogram of I_{aggr} is generated for 1000 snapshots.

ii Using the $I_{\max}$ value, the outage probability $P_{out} = P[I_{aggr} > I_{\max}]$ is calculated and compared against $P_{out,\max}$.
If $P_{out} \leq P_{out,\max}$, then stop; the current value of $d(\theta)$ is the optimum $d_{opt}(\theta)$.
If $P_{out} > P_{out,\max}$, then repeat experiment after incrementing $d(\theta)$ by $\Delta = 0.5$ km.

iii The above steps are repeated to plot a histogram as shown in Figure 2.19.

The above method is repeated and the distribution of the protection region is found for the non-omni gain pattern described in Section 1.

2.6.1.1 Distribution of protection region

The protection region is calculated 2000 times for $I_{max} = -50$ dBm and $\lambda = 10^{-6}$. This is shown in Figure 2.19. It was found that d_{opt} has a Gaussian fit, and therefore can be characterized as a Gaussian random variable.

2.6.2 Iterative Monte Carlo simulations

In this section, we adopt an adaptive on-line algorithm for updating the values of $d(\theta)$ based on the Adam algorithm proposed in [27]. Adaptive moment estimation (Adam) computes an adaptive learning rates for each parameter by using an exponentially decaying average of past squared gradients (v_t) and the past gradients (m_t). The algorithm steps are outlined below:

i The gradient is chosen as $g_t = P_{out} - P_{out,max}$.

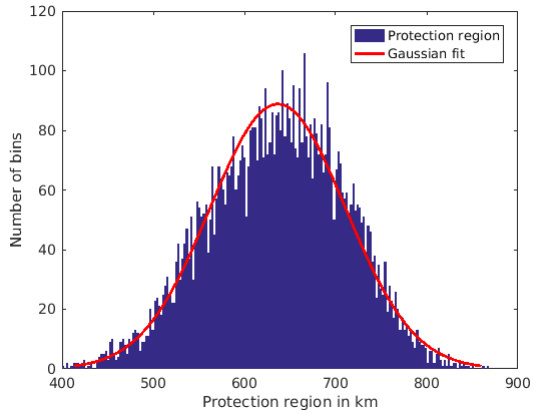

Figure 2.19: Numerical Brute Force: P.D.F. of d_{opt} with mean 637.64 km and standard deviation 74.41 km

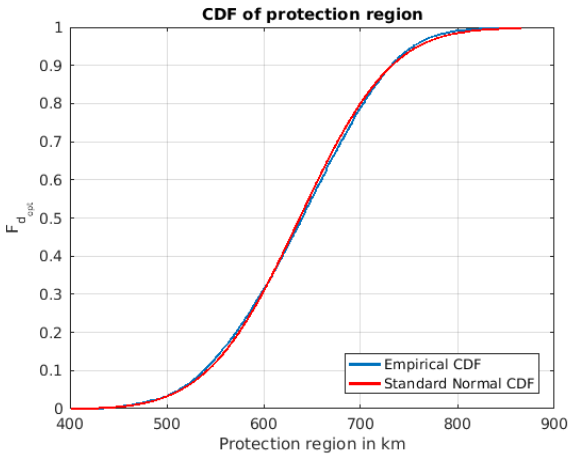

Figure 2.20: C.D.F. of d_{opt}

ii Initialize: Stepsize $\alpha = 50$, $\beta_1 = 0.9, \beta_2 = 0.999$ and $\epsilon = 10^{-8}$.

iii The first moment vector (m), second moment vector (v) and timestep vector (t) are initialized as

$m \leftarrow 0, v \leftarrow 0, t \leftarrow 0$ and $d(\theta) = 10$ km.

iv **while** $d(\theta)$ has not converged, **do**

$t \leftarrow t + 1$

run Monte Carlo experiment 10000 times to obtain P_{out-t}

$g_t \leftarrow P_{out-t} - P_{out,\max}$

$m_t \leftarrow \beta_1 m_{t-1} + (1 - \beta_1) g_t$

$v_t \leftarrow \beta_2 v_{t-1} + (1 - \beta_2) g_t^2$

$\alpha_t \leftarrow \alpha(1 - \beta_2^t)^{\frac{1}{2}}/(1 - \beta_1^t)$

$\hat{m}_t \leftarrow \beta_1 m_{t-1} + (1 - \beta_1) g_t$

$\hat{v}_t \leftarrow \beta_2 v_{t-1} + (1 - \beta_2) g_t^2$

$d(\theta)_t \leftarrow d(\theta)_{t-1} - \alpha_t \hat{m}_t/(\hat{v}_t)^{\frac{1}{2}} + \epsilon)$

end while

v stop: $d(\theta)_t$ is optimal protection distance

In order to check convergence at each iteration, a histogram of I_{aggr} is generated, using 10000 snapshot results for a given value of $d(\theta)$. Using $I_{\max}$ value, the outage probability ($P_{out} = P[I_{aggr} > I_{\max}]$) is calculated and compared against $P_{out,\max}$. If $|P_{out} - P_{out,\max}| \leq \delta = 0.001$, then algorithm stops; keeping current value of $d(\theta)$ as $d_{opt}(\theta)$.

2.6.2.1 Distribution of protection region

The protection region is calculated 5000 times for $I_{max} = -50$ dBm and $\lambda = 10^{-6}$. This is shown as a histogram in Figure 2.21.

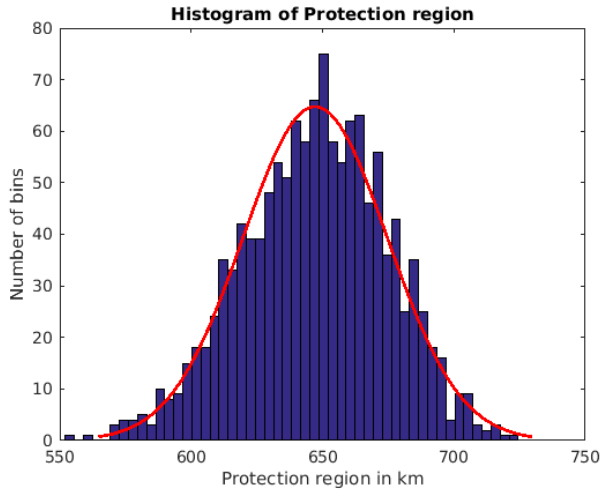

Figure 2.21: Iterative Monte Carlo: P.D.F of d_{opt} with mean 645.65 km and standard deviation 27.25 km

2.7 WLAN Network Activity and its Implications

2.7.1 Part 1 - All co-channel WLAN Networks are non-overlapping

The number of Wi-Fi nodes associated with an access point affects the WLAN network activity. In order to model network activity, some assumptions are made:

(a) The number of nodes associated with an AP is fixed, and each node always has a packet for transmission (saturation condition).

(b) Regardless of the number of retransmissions that a packet may have already suffered, the collision probability of a packet transmitted by each node is assumed to be independent and constant.

(c) Packet errors occur only due to transmission collisions, i.e. the channel conditions are ideal. Also, there are no hidden nodes considered in the analysis.

To use these results, the access points must be distributed such that no two co-channel cells overlap with high probability.

A stationary Poisson point process Φ of intensity λ_{AP} is characterized by

$$P(\Phi(A) = n) = \frac{(\lambda_{AP}|A|)^n}{n!} e^{-\lambda_{AP}|A|} \tag{2.30}$$

Let

$$P(\Phi(\pi r_{CS}^2) > 1) < 0.1 \tag{2.31}$$

where r_{CS} is the *carrier sense range* of an access point.

Carrier sensing range is the range within which the other stations can sense transmitted power. From the IEEE standard for 802.11g, a receiver sensitivity of -87 dBm is chosen as the threshold for carrier sense range. For a free-space path loss exponent 4, the carrier sense range is 266 m.

This implies

$$P(\Phi(\pi r_{CS}^2) = 0) + P(\Phi(\pi r_{CS}^2) = 1) > 0.9 \tag{2.32}$$

$$e^{-\lambda_{AP}\pi r_{CS}^2} + \lambda_{AP}\pi r_{CS}^2 e^{-\lambda_{AP}\pi r_{CS}^2} > 0.9 \tag{2.33}$$

On solving we get

$$\lambda_{AP} < \frac{-W_{-1}(\frac{-9}{10e}) - 1}{\pi r_{CS}^2} \tag{2.34}$$

where $W_k(z)$ is the analytic continuation of the product log function (Lambert W function). From [22], the probability τ that a station transmits in a randomly chosen time slot is found. For simplicity, the constant backoff window problem is considered. That is, the number of backoff stages $m = 0$. In this case,

$$\tau = \frac{2}{W+1} \tag{2.35}$$

where W is the contention window.

In every Wi-Fi network, let P_{tr} be the probability that there is at least one transmission in a randomly chosen time slot. If n stations contend on the channel, and each transmits with probability τ,

$$P_{tr}(n) = 1 - (1-\tau)^n \tag{2.36}$$

From the perspective of coexistence between a radar and Wi-Fi networks, the number of

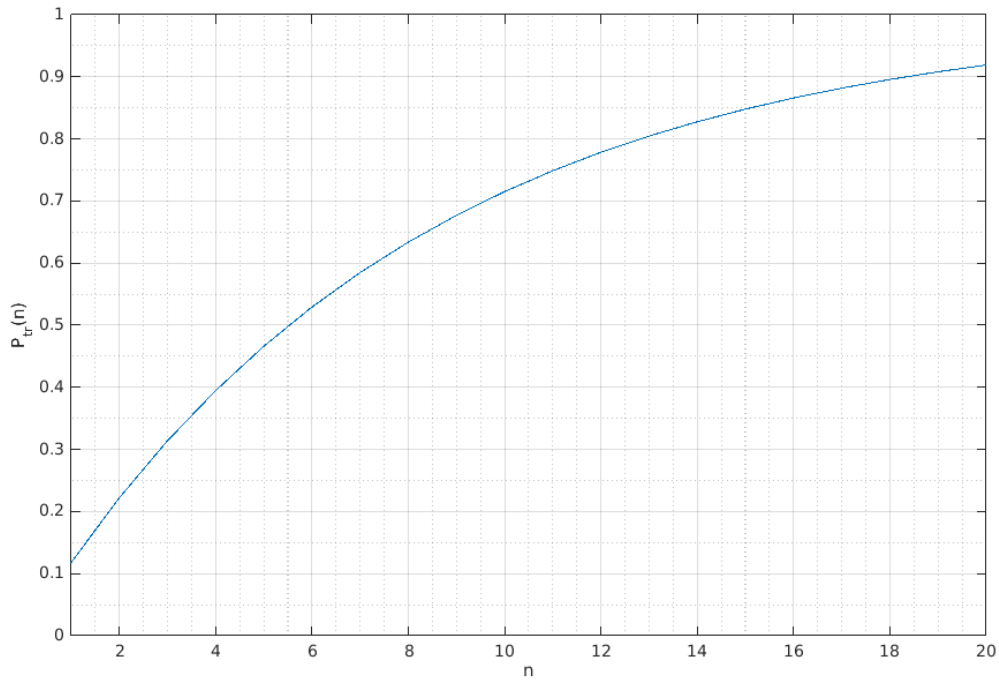

Figure 2.22: P_{tr} vs n

transmissions in a Wi-Fi network directly impact the total interference at the radar receiver. By increasing the number of clients associated with a Wi-Fi AP, the probability that there is at least one transmission in a randomly chosen time slot is given in Figure 2.22.

2.7.1.1 Characterization of aggregate interference at Radar

The aggregate interference from secondary users to radar (located at y) is described as a generalized shot noise process in space as shown in (2.37). It is assumed that every AP is independently active with probability p. In this thesis, this probability is characterized according to (2.36).

$$I_{aggr}(y) = \sum_{x \in \Phi} \frac{P_x G(\theta_x)}{\mathrm{FDR}(\Delta f)} l(||y - x||) \tag{2.37}$$

where P_x is the SU transmit power at AP location x and $||y - x||$ describes the distance between radar and secondary access point. The transmit power for all Wi-Fi networks is assumed to be fixed, $P_x = P_{SU}$. $l(.)$ is the impulse response function that models signal attenuation (inverse of path loss). For a PPP of density λ, the mean and variance of the sum $\sum_{x \in \Phi} f(x)$ is calculated from Campbell's theorem as

$$E[\sum_{x \in \Phi} f(x)] = \lambda \int_{\mathcal{R}^d} f(x) dx \tag{2.38}$$

$$var[\sum_{x \in \Phi} f(x)] = \lambda \int_{\mathcal{R}^d} f^2(x) dx \tag{2.39}$$

The average interference is calculated using (8) by integrating over the two dimensional plane. It is assumed that the radar receiver is at the origin, i.e. $y = 0$.

$$\mu_{I_{aggr}} = E[I_{aggr}] = \frac{p \lambda P_{SU}}{\mathrm{FDR}(\Delta f)} \int_{\mathcal{R}^2} G(\theta_x) l(||x||) dx \tag{2.40}$$

Here, each network is independently active with probability p. In this thesis, this is calculated according to (7).

A minimum separation distance between radar and SU as a function of θ, $d(\theta)$. Using polar coordinates and considering Longley Rice path loss model $l(r) = K_0 r^{-\alpha}$,

$$\mu_{I_{aggr}} = \frac{p \lambda P_{SU} K_0}{\mathrm{FDR}(\Delta f)} \int_{\theta} \int_{d(\theta)}^{\infty} G(\theta) r^{1-\alpha} dr d\theta = \frac{p \lambda P_{SU} K_0}{\mathrm{FDR}(\Delta f)(\alpha - 2)} \int_{\theta} G(\theta) d^{2-\alpha}(\theta) d\theta \tag{2.41}$$

Similarly, the variance is calculated as

$$\sigma^2_{I_{aggr}} = \frac{p\lambda P^2_{SU} K^2_0}{\mathrm{FDR}^2(\Delta f)} \int_\theta \int_{d(\theta)}^{\infty} G^2(\theta) r^{1-\alpha} dr d\theta = \frac{p\lambda P^2_{SU} K^2_0}{\mathrm{FDR}^2(\Delta f)(2\alpha - 2)} \int_\theta G^2(\theta) d^{2-\alpha}(\theta) d\theta \quad (2.42)$$

The Wi-Fi APs are represented by a PPP Φ with density λ_{AP} and is characterized below.

$$P(\Phi(A) = n) = \frac{(P_{tr}(M)\lambda_{AP}|A|)^n}{n!} e^{-P_{tr}(M)\lambda_{AP}|A|} \quad (2.43)$$

The number of stations associated with an access point is a Poisson random variable M with intensity λ_{node}. (2.7) is re-written for $P_{tr}(M)$ as

$$P_{tr}(M) = 1 - (1 - \tau)^M \quad (2.44)$$

The interference caused by one Wi-Fi network at the radar receiver is given by

$$I(y|M = m) = \frac{P_{tr}(m) P_x G(\theta_x)}{\mathrm{FDR}(\Delta f)} l(||y - x||) \quad (2.45)$$

where $m \in M$ and $x \in \Phi$.

Therefore, (2.37) is re-written as

$$I_{aggr}(y) = \sum_{m \in M} P(M = m) I(y|M = m) \quad (2.46)$$

where

$$P(M = m) = \frac{(\lambda_{node})^m}{m!} e^{-\lambda_{node}} \quad (2.47)$$

By conditioning on M in (2.43) we get

$$P(\Phi(A) = n|M = m) = \frac{(1 - (1 - \tau)^m)\lambda_{AP}|A|)^n}{n!} e^{-(1-(1-\tau)^m)\lambda_{AP}|A|} \quad (2.48)$$

To express (2.43) using the above equation,

$$P(\Phi(A_1) = n) = \sum_{m=0}^{\infty} P(\Phi(A_1) = n|M = m) P(M(A_2) = m) \quad (2.49)$$

where A_1 is the area considered around the radar (city or town) and A_2 is the circular area around the access point with radius r_{CS} (i.e. $A_2 = \pi r^2_{CS}$).

$$P(\Phi(A_1) = n) = \sum_{m=0}^{\infty} \frac{(1 - (1 - \tau)^m)\lambda_{AP}|A_1|)^n}{n!} e^{-(1-(1-\tau)^m)\lambda_{AP}|A_1|} \frac{(\lambda_{node}|A_2|)^m}{m!} e^{-\lambda_{node}|A_2|} \quad (2.50)$$

2.7.2 Part 2: Overlapping co-channel WLAN Networks

In this subsection, we consider downlink traffic, i.e., packets sent from the APs to the associated nodes. We also assume that it is equally likely for the AP to transmit to all the nodes. In these scenarios, the location of the neighbouring APs determine the network activity. Consider Figure 2.23, the neighbouring APs are within the carrier-sense range. P_{tr}, i.e. the probability that there is at least one transmission in a randomly chosen time slot is given by (2.51) where n_1 and n_2 are the number of nodes (stations) associated with AP_1 and AP_2 respectively. Similar to the previous section, nodes contend on the channel, and each receives a packet with probability τ,

$$P_{tr}(n) = 1 - (1 - \tau)^{n_1+n_2} \tag{2.51}$$

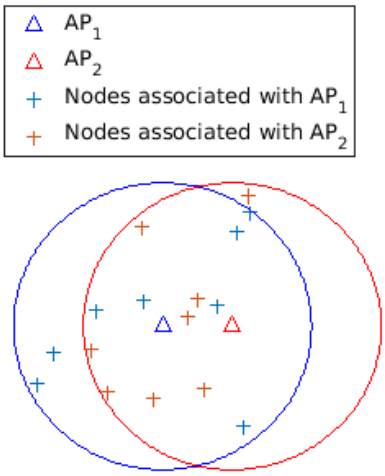

Figure 2.23: Neighbouring APs within carrier-sense range

To find the average number of active links is a dense Wi-Fi AP deployments, the following algorithm is used:

i Draw circles with radius equal to the carrier sense range by a applying a suitable circle packing algorithm [23] in the considered 2-D space.

ii If APs lie inside a circle, then it is assumed that they are all within carrier sense range of each other.

iii If APs lie outside all the circles, they are associated to the nearest circle in their vicinity.

iv The number of circles with APs inside them correspond to the number of active links at a given time instant.

In the previous sections, we assumed that all the APs are simultaneously active at a given instant of time. By using the algorithm provided in this section we can find the number of Wi-Fi APs that have an active link. Figures 2.24, 2.25 and 2.26 show the above algorithm being used to find the number of active links for a given λ_{AP}. The λ_{AP} values are relevant with real-world datasets as explained in the next section.

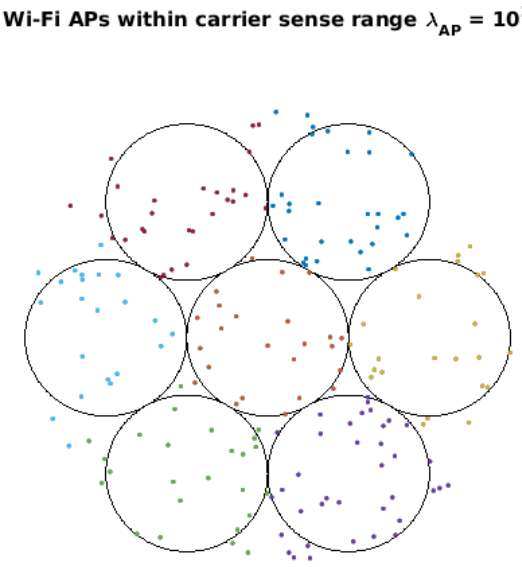

Figure 2.24: On average, only 5% of the APs are active

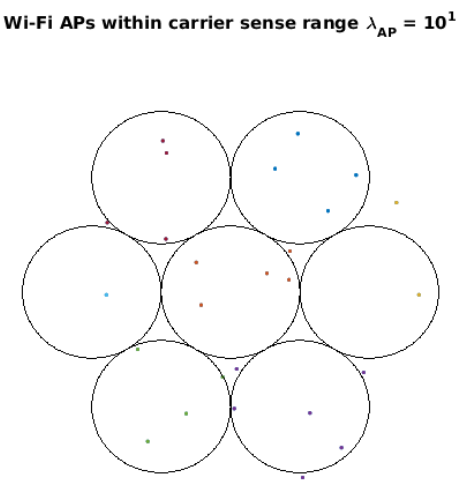

Figure 2.25: On average, only 32% of the APs are active

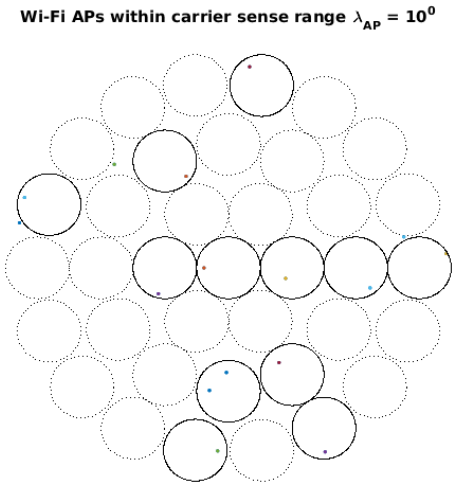

Figure 2.26: On average, 85% of the APs are active

2.8 Real-world example

A sophisticated software program was designed to compute protection regions in the US. The determination of protection regions is impacted by a multiplicity of factors on both the secondary (notably, the transmit power, deployment geometry, transmit antenna patterns) and primary (receiver sensitivity and operational margins, receive antenna patterns) side as well as the channel characteristics (distance and frequency dependant pathloss, and any statistical effects such as small-scale fading and large-scale shadowing).

2.8.1 Path loss model and Propagation losses

In this analysis, the channel characteristics were modeled using the Longley-Rice path loss model [24]. The topological terrain was taken from SRTM-3, an international research effort that resulted in the most high-resolution digital topological database of Earth. Using the Longley Rice model would therefore provide a very accurate computation of the path loss. The propagation losses considered are building attenuation losses mentioned in [12]. It is assumed that 90 percent of the APs and associated clients will operate indoors. The transmit

power for outdoor and indoor APs is chosen as 30 dBm and 23 dBm respectively. For the indoor APs, a building attenuation loss in addition to the propagation loss was used in the protection region computation. The following random distribution was used to represent the building attenuation loss in the analysis: 20 percent were assigned a building attenuation loss of 20 dB; 60 percent were assigned a building attenuation loss of 15 dB; and 20 percent were assigned a building attenuation loss of 10 dB.

2.8.2 Location of WLANs and Network activity

Various open-source databases [25] provide locations (in terms of latitudes and longitudes) of WLANs across the world. These databases are populated by known research efforts and mobile applications that send AP information for users. Using the datasets, the locations of the active APs in the US was used for the protection region computation. Around 9 million locations were considered for the US as shown in Figure 2.27 using the Mercator projection [26]. Since we are interested in the number of Wi-Fi APs that are co-channel to the Radar, the channel used by the Wi-Fi APs is crucial. The dataset has an aggregation of APs in all channels, and the percentage of APs in the given channels are shown in Table 2.9. By considering WLANs in the 2.4 GHz bands (Channels 1, 6 and 11), we assume that 20% of the APs are co-channel to the Radar.

Table 2.9: Dataset - Percentage of APs in the given WLAN channel

Channel	Percentage of Wi-Fi APs
1	21.79
6	21.75
11	19.66
Other	26.69
Unknown	10.11

Figure 2.27: Each black dot represents one location of a Wi-Fi AP

Using the location of the Wi-Fi APs, λ_{AP} values were estimated for various areas along the West coast of the US. This is shown in Table 2.10. The main takeaway from this analysis is that if WLANs are deployed to coexist with Radars, the density of these deployments can be similar to the density of networks currently being operated in the 2.4 GHz bands.

2.8.3 Determination of Protection region

The determination of the protection region is deterministic for a given main beam direction of the Radar for a given deployment. Using the given dataset and the algorithms described in this chapter, a realistic computation of the protection region can be obtained by assuming that the location and main-beam direction of the Radar is known. Then, the mobile operators can synchronize with WLANs across cities to operate based on the protection regions specified. In reality, the location and mainbeam direction of the Radar is not known. In the next chapter, we estimate these unknown parameters.

Table 2.10: λ_{AP} values along the West coast

Area	Type of area	λ_{AP} (per sq. km)
San Francisco (SF)	Dense Urban	$1.45\text{x}10^{2}$
Seattle (SEA)	Dense Urban	$8.12\text{x}10^{1}$
Los Angeles (LA)	Dense Urban	$8.35\text{x}10^{1}$
Portland	Dense Urban	$1.12\text{x}10^{1}$
SF Bay area	Urban	$5.01\text{x}10^{0}$
SEA Metropolitan	Urban	$6.05\text{x}10^{0}$
LA Metropolitan	Urban	$4.08\text{x}10^{0}$
Coastline between SF and LA	Suburban	$4\text{x}10^{-2}$
Coastline between SF and Portland	Suburban	$2\text{x}10^{-3}$
Washington (excluding Seattle Metropolitan area)	Suburban	$7.3\text{x}10^{-3}$
Oregon and Idaho (excluding Portland and coastline)	Rural	$6.9\text{x}10^{-4}$
Nevada (excluding Las Vegas)	Rural	$6.3\text{x}10^{-5}$

Chapter 3

ESTIMATION OF RADAR PARAMETERS USING WI-FI USERS

3.1 Introduction

Radars are mainly used for military, weather and air-traffic control. Due to the sensitive nature of Radar operation, the instantaneous location and main beam direction are not revealed. In Chapter 2, all the studies rely on the assumption that these parameters are known. Here, a method to predict these parameters and characterize the implications on the protection region are discussed. The assumptions made here are that there is no synchronization between the Radar and WLANs.

3.2 Prediction of Main Beam Direction

3.2.1 System Set-up and Dataset generation

The Radar is placed at a known location. Around it, the Wi-Fi users are scattered according to a homogeneous Poisson point process as shown in Figure 3.1.

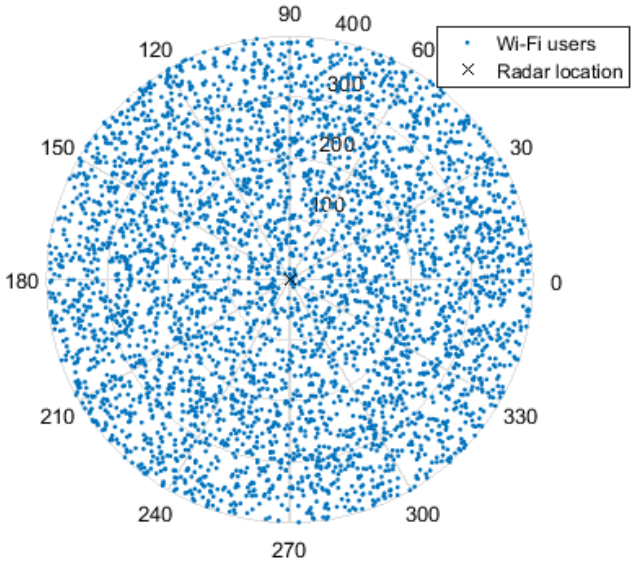

Figure 3.1: Homogeneous PPP with intensity $\lambda = 10^{-2}$

The antenna gain and Wi-Fi specifications are taken from (2.29) and [9]. Figure 3.3 shows antenna gain versus azimuth with a main lobe value of 33.5 dBi.

At the Wi-Fi receiver, the radar signal is treated as interference. The effective interference-to-noise ratio at the receiver is calculated according to (3.1) whose values are taken from [28].

$$\mathrm{INR}_{eff} = 10 \log_{10} \left(\frac{PW f_R P_T G_w G(\theta) l(r)}{N_0 BW} \right) \tag{3.1}$$

where $l(d) = K_0 r^{-\alpha}$ is the path loss model between radar and Wi-Fi receiver [9], d is the distance between radar and Wi-Fi receiver, G_w is the antenna gain of the Wi-Fi access point and BW is the Wi-Fi channel bandwidth. P_T is the power of the transmitted radar signal and f_R is the pulse repetition frequency.

For a given main beam direction, the Wi-Fi users detect the Radar signal during normal operation, with a probability of detection given in [28]. This is shown in Figure 3.2. By considering the probability of detection during normal operation of Wi-Fi, we assume the *worst-case scenario* in terms of the number of users that detect the signal. If Wi-Fi users were idle and sensing the channel for Radar transmissions, the probability of detection will be higher.

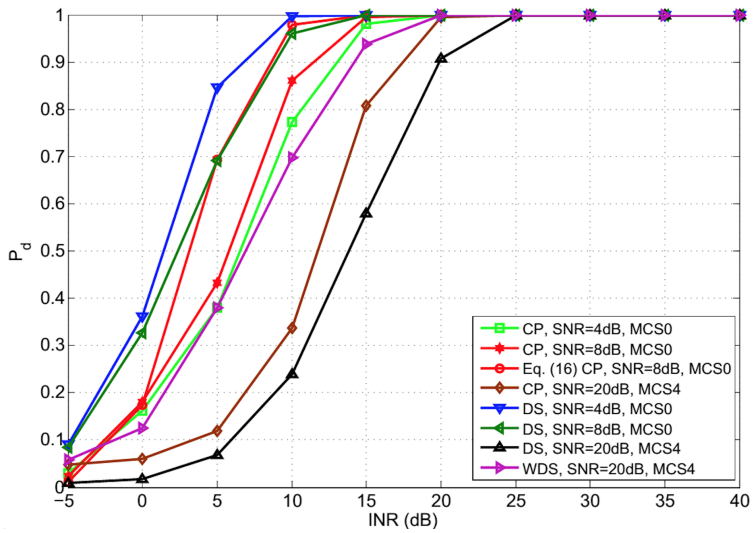

Figure 3.2: The CP, MCS4 specification is chosen for the dataset generation

The algorithm steps are outlined below:

i A random Radar location and main beam direction is chosen.

ii Using the antenna gain in (2.29), we compute the INR_{eff} at every Wi-Fi receiver using (3.1).

iii To choose the subset of all Wi-Fi APs that have detected the Radar signal, the following decision is made.

An AP is chosen with a probability of detection given by the results in [28], i.e., Figure 2. Once this operation is complete, we have the set of all Wi-Fi receivers that have detected the Radar signal.

iv The true location of the Radar, the true main beam direction of the Radar and the location of all the Wi-Fi APs form one dataset. One realization of a dataset is shown in Figure 3.4.

v The above operation is repeated 10000 times to obtain a dataset with 10000 realizations.

At a given time instant, the set of all Wi-Fi users that detect the Radar signal report their locations to a data center. One realization of this is shown in Figure 3.4.

The data center implements the technique described in this paper, using the location of these users.

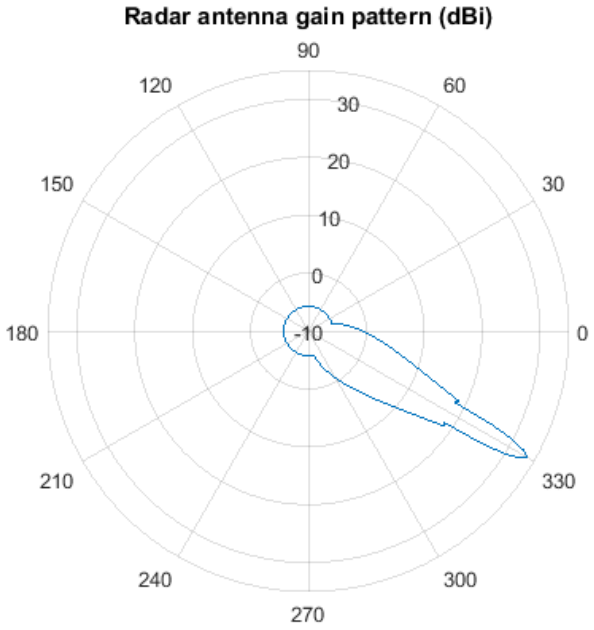

Figure 3.3: Radar Antenna Gain pattern with $\theta_M = -\frac{\pi}{6}$

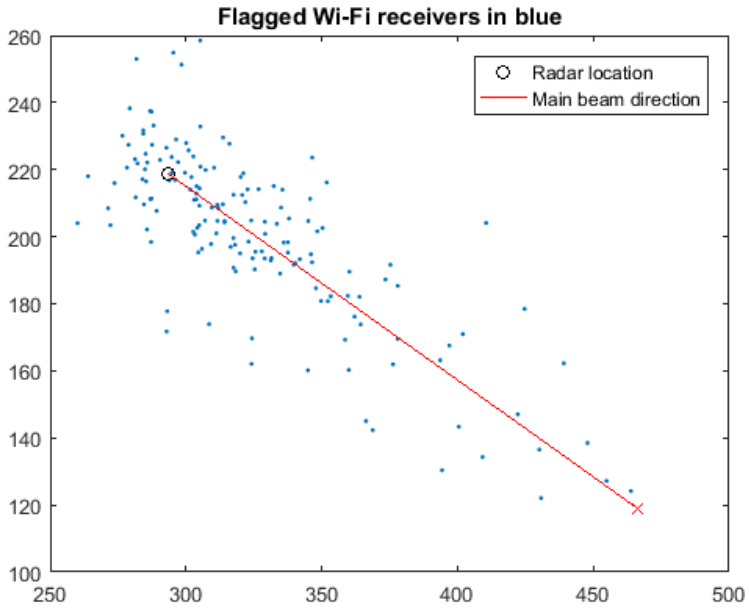

Figure 3.4: The Radar location, main beam direction and Wi-Fi user locations comprise the dataset

3.2.2 Simulation set-up

For a radar receiver located at the origin, Wi-Fi nodes are scattered according to a PPP with density $\lambda = 10^{-6}$. The total area of deployment is a circle with outer radius of 5,000 km.

Secondary user power (including its antenna gain) is set to $P_{su} = 1.0$ watt, in line with commercial Wi-Fi devices. We consider a path-loss component of $\alpha = 4$ and outage probability of $P_{out,\max} = 0.1$.

3.2.3 Huber M-estimator

The objective function of the Huber M-estimator [29] is given below and shown in Figure 3.5.

$$\rho(e) = \begin{cases} \frac{1}{2}e^2 & |e| \leq k \\ k|e| - \frac{1}{2}k^2 & |e| > k \end{cases} \tag{3.2}$$

To choose the value of k, the following algorithm was used.

i Initialize $k = 0.1, \delta = 0.1$.

ii For a given realization of the dataset, the line of best fit is the line that minimizes the objective function ρ in (3.2).

iii **while** ρ has not been minimized, **do**

$k \leftarrow k + \delta$

$t \leftarrow t + 1$

Compute minimum $(\rho)_t$

If $(\rho)_t < (\rho)_{t-1}$: $\rho \leftarrow (\rho)_t$

end while

iv stop: ρ is minimized, and corresponding value of k is used for every dataset.

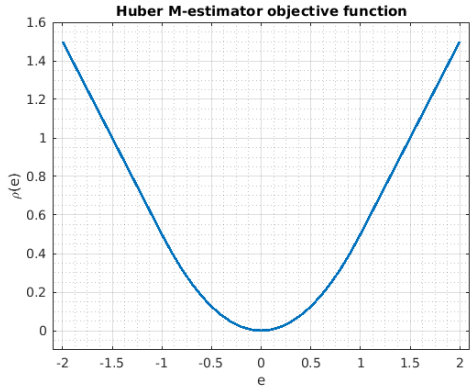

Figure 3.5: Objective function for $k = 1$.

3.2.4 Error in Main beam direction

The error in main beam direction was computed by using the Huber M-estimator as the predicted direction of the main beam. The error is given by the angle between the true main beam direction and the predicted main beam direction. For 10000 observations, a histogram of the error was computed and modelled as a Gaussian random variable with mean -0.001 and $\sigma = 2.865$ degrees. It is shown in Figure 3.6.

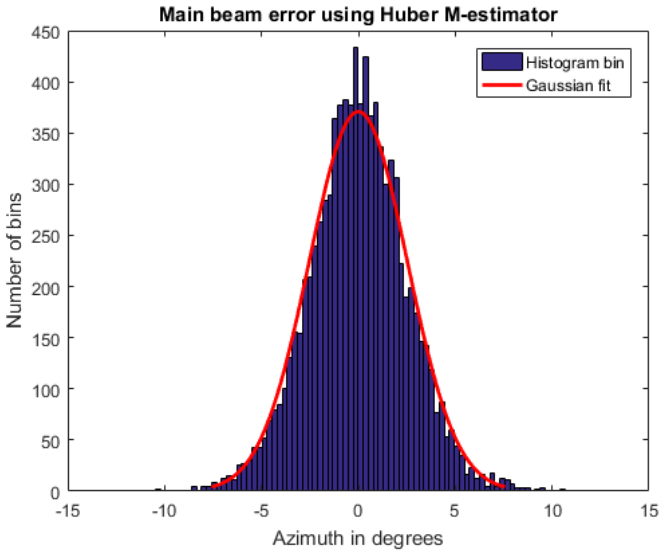

Figure 3.6: Histogram of error

3.2.4.1 Gaussian assumption for distribution of I_{aggr}

In [9], the distribution of I_{aggr} was approximated as a normal distribution $N(\mu_I, \sigma_I^2)$, as it allows further inroads towards an analytical determination of the optimum protection region as summarized below. With the Gaussian assumption, the outage probability can be determined as

$$P_{outage} = \Pr\{I_{aggr} > I_{\max}\} = Q\left(\frac{I_{\max} - \mu_I}{\sigma_I}\right) \tag{3.3}$$

where $Q(.)$ function is the tail probability of the standard normal distribution. It is desired to set an upper bound for probability of outage, $P_{out,\max}$, i.e.,

$$P_{outage} \leq P_{out,\max} \rightarrow Q\left(\frac{I_{\max} - \mu_I}{\sigma_I}\right) \leq P_{out,\max}$$

$$I_{\max} \geq \mu_I + \sigma_I Q^{-1}\left(P_{out,\max}\right) \tag{3.4}$$

Here, the coexistence criteria is defined by (3.4). This inequality is trivially achieved by letting $d(\theta) \rightarrow \infty$. In order to avoid this, we *minimize the total protection area* subject to net interference limit as formulated in following optimization problem:

$$d_{opt} = \arg\min_{d(\theta)} \int_0^{2\pi} d^2(\theta) d\theta \tag{3.5}$$

subject to:

$$\mu_I + \sigma_I Q^{-1}\left(P_{out,\max}\right) \leq I_{\max} \tag{3.6}$$

For a general antenna pattern $G(\theta)$, it is proven in the appendix that optimum protection distance $d_{opt}(\theta)$ is proportional to $G^{1/\alpha}(\theta)$ with a constant γ that is determined by numerically solving following equation:

$$d_{opt}(\theta) = \gamma G^{\frac{1}{\alpha}}(\theta) \qquad \text{where} \tag{3.7}$$

$$\mathcal{A}\gamma^{2-\alpha} + \mathcal{B}\gamma^{1-\alpha} - I_{\max} = 0 \tag{3.8}$$

in which $\mathcal{A}$ and $\mathcal{B}$ are determined by:

$$\mathcal{A} = C_{\mu_I} \int_0^{2\pi} G^{\frac{2}{\alpha}}(\theta) d\theta$$

$$\mathcal{B} = Q^{-1}\left(P_{out,\max}\right) \sqrt{C_{\sigma_I^2} \int_0^{2\pi} G^{\frac{2}{\alpha}}(\theta) d\theta} \tag{3.9}$$

3.2.5 Distribution of $d_{opt}(\theta)$

Let the error in the main beam direction be a Gaussian random variable $\epsilon \sim \mathcal{N}(0, \sigma_m^2)$ given in Figure 3.6. In the presence of ϵ, (3.7) is re-written as

$$d_{opt}(\theta + \epsilon) = \gamma G^{\frac{1}{\alpha}}(\theta + \epsilon) \tag{3.10}$$

Using Taylor series expansion of $G^{\frac{1}{\alpha}}(\theta + \epsilon)$ we get

$$d_{opt}(\theta + \epsilon) = \gamma \left[G(\theta) + \epsilon G^{(1)}(\theta) + \frac{\epsilon^2}{2} G^{(2)}(\theta) + \frac{\epsilon^3}{6} G^{(3)}(\theta) + \mathcal{O}(h^4) \right]^{\frac{1}{\alpha}} \tag{3.11}$$

$$d_{opt}(\theta + \epsilon) \simeq \gamma \left[G(\theta) + \epsilon G^{(1)}(\theta) \right]^{\frac{1}{\alpha}} \tag{3.12}$$

by approximating to the first-degree. Further, by using Binomial approximation we get

$$d_{opt}(\theta + \epsilon) = \gamma G(\theta)^{\frac{1}{\alpha}} \left[1 + \epsilon \frac{G^{(1)}(\theta)}{G(\theta)} \right]^{\frac{1}{\alpha}} \tag{3.13}$$

$$d_{opt}(\theta + \epsilon) \simeq \gamma G(\theta)^{\frac{1}{\alpha}} \left[1 + \frac{\epsilon}{\alpha} \frac{G^{(1)}(\theta)}{G(\theta)} \right] \tag{3.14}$$

for $\alpha > 1$ and $G^{(1)}(\theta) < G(\theta)$.

This implies that $d_{opt}(\theta + \epsilon)$ has a Gaussian distribution, i.e.

$$d_{opt}(\theta + \epsilon) \sim \mathcal{N}\left(d_{opt}(\theta), [\frac{\sigma_m}{\alpha} \frac{G^{(1)}(\theta)}{G(\theta)}]^2 \right)$$

.

3.3 Prediction of Location

The simulation set-up is described in the previous section. Here, using the predicted main beam direction of the Radar, a prediction for the location is made.

3.3.1 Dataset

The dataset used to evaluate the error in location of the Radar is same as the previous section (Figure 3.4).

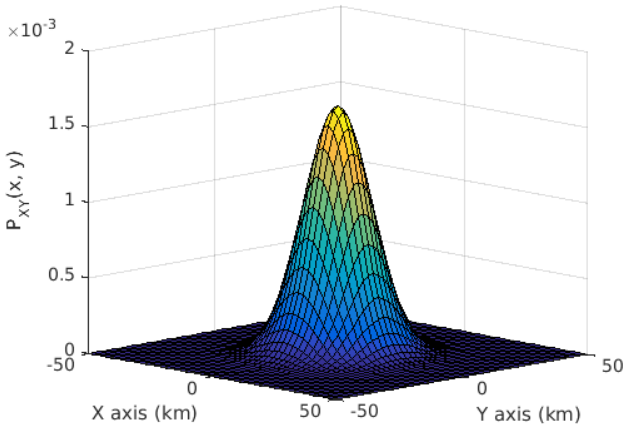

Figure 3.7: 2-D Gaussian histogram plot

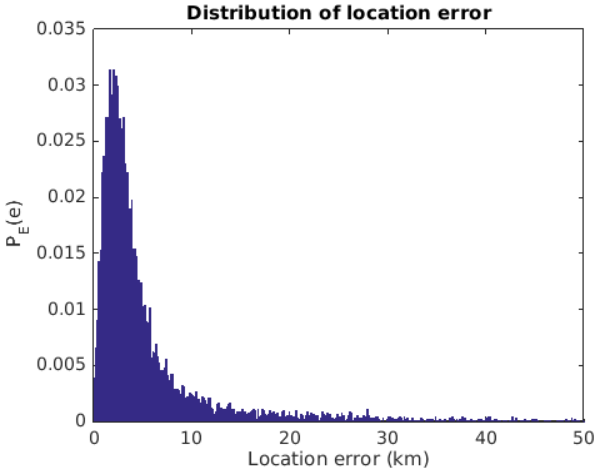

Figure 3.8: Location error is the difference between true location and the predicted location

3.3.2 Two regression lines at random angles

If we draw two regression lines using the m-estimator at random angles, the point of intersection of these lines is chosen as the location of the Radar.

The predicted location of the radar has a 2-D Gaussian distribution with

$$\mu = \begin{bmatrix} -0.16 \\ -0.11 \end{bmatrix}, \Sigma = \begin{bmatrix} 95.70 & 0.28 \\ 0.28 & 97.91 \end{bmatrix}$$

where the $\begin{bmatrix} 0 \\ 0 \end{bmatrix}$ is the true location of the radar. A histogram of the distance to the points from the mean of the 2-D Gaussian distribution is plotted in Figure 3.8.

3.3.3 N regression lines at random angles

By choosing angles randomly, multiple lines drawn may be parallel to each other (Figures 3.9 and 3.10). This will increase the location error. To quantify this, we use the root-mean squared error (RMSE). Using the RMSE as the performance metric, we find the optimal

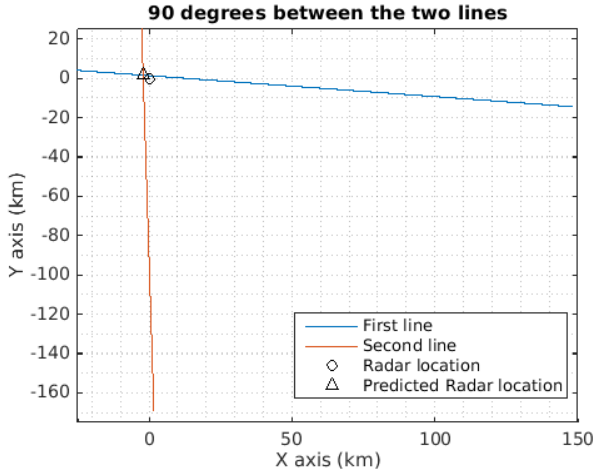

Figure 3.9: 90 degrees is the optimal angle for two lines

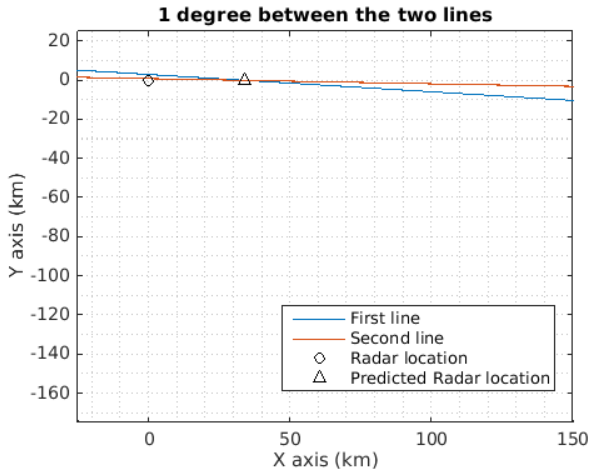

Figure 3.10: The angle between the lines play a role in accurate localization

angle to choose between any two lines. It is found that 90 degrees is the optimal angle when we choose to construct two lines. This is shown in Figure 3.11.

$$\text{RMSE} = \sqrt{\frac{1}{N}\sum_{i=1}^{N}(y_i - \hat{y}_i)^2}$$

where y_i and $\hat{y}_i$ are the location of the Radar and predicted location of the Radar.

3.3.4 N regression lines at $\frac{\pi}{N}$ angles

By choosing the lines at $\frac{\pi}{N}$ angles, we improve the accuracy of our prediction of the Radar location. This is shown in Figure 3.15. Further, we compare the results obtained in this section with the previous section in Table 3.1, i.e. to compare the effect of choosing angles at $\frac{\pi}{N}$ radians, versus choosing the angles at random.

3.3.5 Protection region due to location error

The implication of the location error on the average protection region was shown using simulations in Figure 3.16. The following algorithm was used to determine the same.

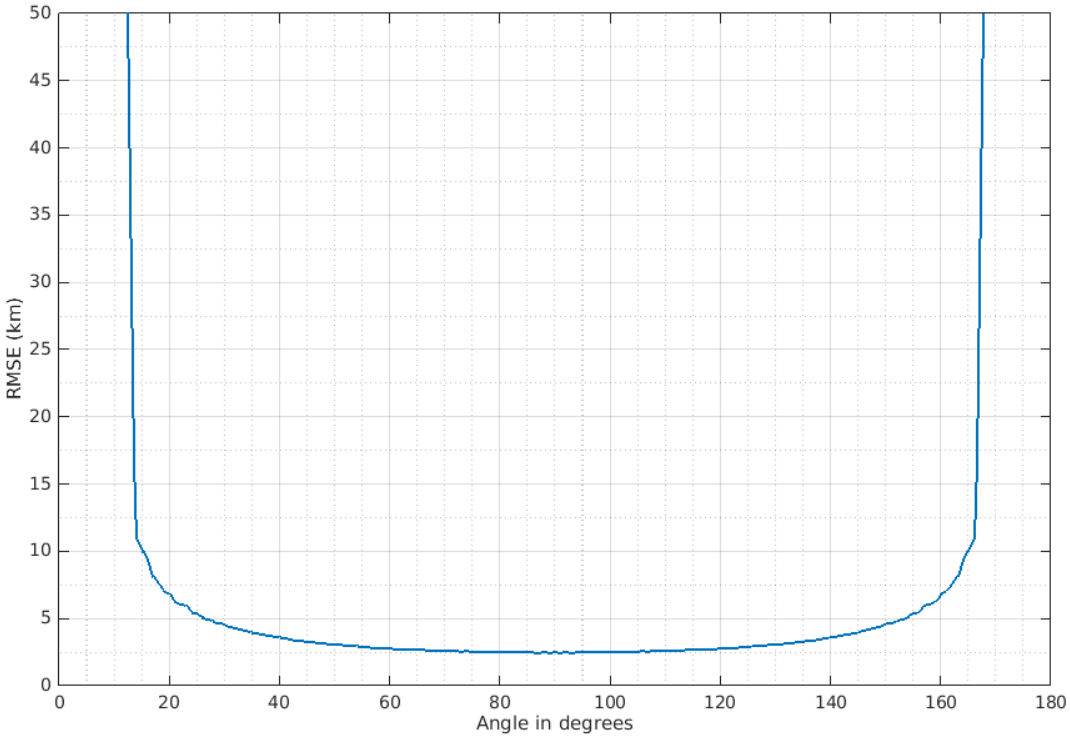

Figure 3.11: RMSE of location estimator vs. Angle between the two lines.

Table 3.1: RMSE comparison

Number of lines	RMSE (km) Lines at random angles	RMSE (km) Lines at $\frac{\pi}{N}$ radians
2	8.592	2.516
3	7.150	2.108
5	5.385	1.760
10	3.316	1.491

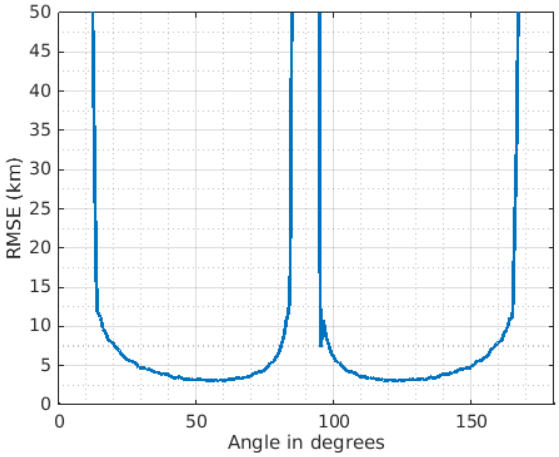

Figure 3.12: Three lines - RMSE vs Angles between successive lines. 60 degrees is the optimal angle

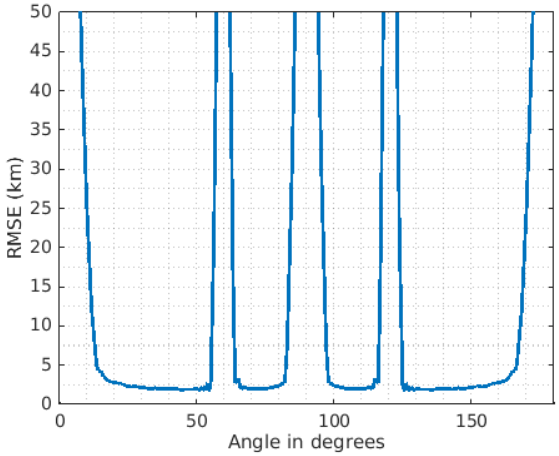

Figure 3.13: Four lines - RMSE vs Angles between successive lines. 45 degrees is the optimal angle

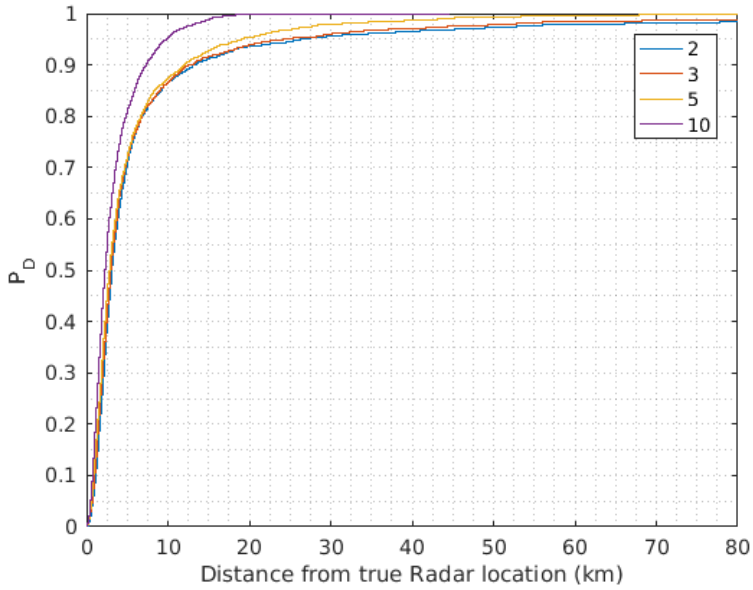

Figure 3.14: Probability of detection of Radar at a given distance from predicted location

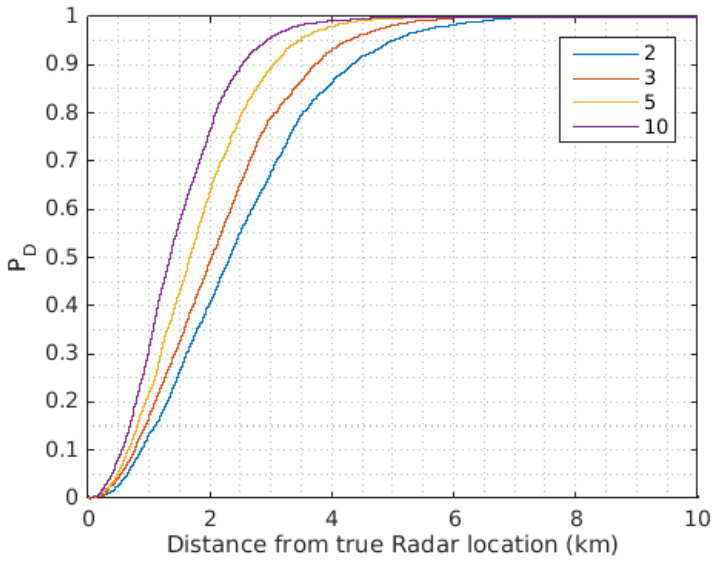

Figure 3.15: Probability of detection of Radar at a given distance from predicted location

i A 2-D Gaussian distribution is used to determine the Radar location. It is assumed that the main beam direction is known.

ii Given the Radar location, the d_{opt} is found using the Iterative Monte Carlo simulations.

iii The above steps are repeated with increasing values of σ_L where the covariance matrix of the 2-D Gaussian distribution is $\Sigma = \begin{bmatrix} \sigma_L^2 & 0 \\ 0 & \sigma_L^2 \end{bmatrix}$.

Figure 3.16 shows the increase in the protection region due to the error in location of the Radar. Figure 3.17 shows the increase in protection distance along the main-beam direction with an increase in σ_L.

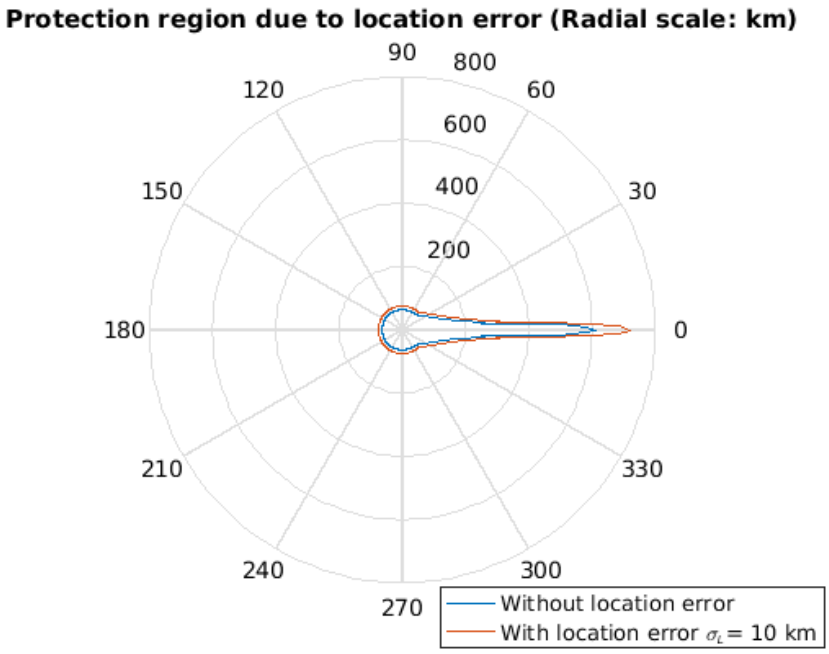

Figure 3.16: Comparison of Protection region with location error

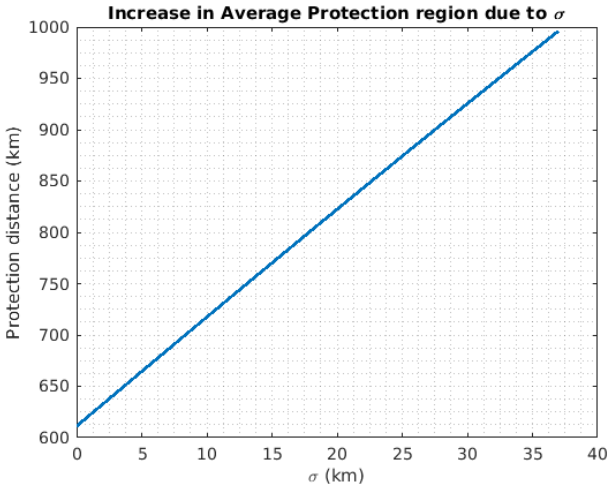

Figure 3.17: Effect of σ_L on the protection region

Chapter 4

CONCLUSIONS AND FUTURE WORK

4.1 Conclusions

The primary objective of our analysis has been to explore the impact of various *stochastic point process models* on I_{aggr}. Since map data for actual real-world deployment of Wi-Fi APs is available, a useful sanity check would be to explore which (or if) the above models represent such deployments. This will potentially result in actual prescriptions for the protection region for a specific metro area, which will be of likely interest to mobile operators. By using an open-source dataset and expecting the deployed networks to be as dense as the networks in the 2.4 GHz bands, we can produce instantaneous computations of the protection region given the Radar location and Mainbeam direction. Further, as noted - I_{aggr} is also impacted by the probability of a wireless network transmitting at a given instant of time, which is related to the MAC protocol employed. Integrating the probability of transmission into the above gives a more complete analysis. Furthermore, it is important to estimate various parameters regarding radar operation (the location of the radar and main beam direction) since this information is not readily known. Extending the analysis to when such parameters are unknown and must be estimated on-line - and its consequent effect on the protection region - is also discussed in this thesis. The analysis emphasizes that the determination of protection regions is significantly impacted by a multiplicity of factors on both the secondary (notably, the transmit power, deployment geometry, transmit antenna patterns) and primary (receiver sensitivity and operational margins, receive antenna patterns) side as well as the channel characteristics (distance and frequency dependant pathloss, and any statistical effects such as small-scale fading and large-scale shadowing).

4.2 Future Work

It is important to compute more accurate Wi-Fi AP densities. This can be done by considering population metrics and building layouts. This allows for a more precise characterization of WLAN network activity and the aggregate interference at the Radar receiver. Also, the path loss model considered in this thesis is obtained from [9]. A more accurate channel model for instantaneous protection region calculation can be obtained by using SRTM-3 (an international research effort that obtained digital elevation models on a global scale to generate the most complete high-resolution digital topographic database of the Earth) with the Longley-Rice pathloss model. To make the WLAN network activity characterization more precise, the exponential backoff scenario can be considered using system-level simulators like NS-3 instead of computing based on the simplistic constant backoff scenario. Since the mainbeam direction is being estimated, this allows for estimating the Radar rotation speed. Although this parameter is not required for protection region calculations, it is an important parameter to estimate for other practical purposes. Another important effort would be to compute the exclusion region along the coastline and compare with NTIA's calculations.

BIBLIOGRAPHY

[1] FCC, ET Docket 08-260, "Second Report and Order and Memorandum Opinion and Order in the Matter of Unlicensed Operation in the TV Broadcast Bands," Nov 14, 2008.

[2] M. Rahman and J. Karlsson, "Feasibility evaluations for secondary lte usage in 2.7-2.9ghz radar bands", *Personal Indoor and Mobile Radio Communications (PIMRC), 2011 IEEE 22nd International Symposium on*, Sept 2011, pp. 525–530.

[3] ITU, "Characteristics of radiolocation radars, and characteristics and protection criteria for sharing studies for aeronautical radionavigation and meteorological radars in the radiodetermination service operating in the frequency band 2700-2900 MHz", Tech. Rep., 2000-2003.

[4] ITU, "Characteristics of and protection criteria for sharing studies for radiolocation, aeronautical radionavigation and meteorological radars operating in the frequency bands between 5250 and 5850 MHz", Tech. Rep. Rec. ITU-R M.1638, 2003.

[5] "Presidential Memorandum: Unleashing the Wireless Broadband Revolution," http://www.whitehouse.gov/the-press-office/presidential-memorandum-unleashing-wireless-broadband-revolution. June 2010.

[6] FCC "Amendment of Commission Rules with regard to commercial operation in 3550-3650 MHz band," Report & Order 15-74A1, 2015.

[7] DARPA STO "Shared Spectrum Access between Rotating Radar and Communications (SSPARC)," BAA 15-24, 2013. https://www.fbo.gov/spg/ODA/DARPA/CMO/DARPA-BAA-15-42/listing.html

[8] R. van Nee and R. Prasad, "OFDM for Wireless Multimedia Communications," Artech House, 2000.

[9] F. Hessar, S. Roy. "Spectrum Sharing Between A Surveillance Radar and Secondary Wi-Fi Networks", *IEEE Trans. on Aerospace and Electronic Systems*, vol. 52, no. 3, pp. 1434-1448, June 2016.

[10] U.S. Dept. of Commerce, "Fast track evaluation of the 5350-5470 MHz and 5850-5925 MHz bands pursuant to section 6406(b) of the middle class tax relief and job creation act of 2012," NTIA, Washington, DC, USA, Tech. Rep., Jan. 2013.

[11] ETSI, EN 301 893, doc REN/BRAN-0060011, pp. 1–26, 2012.

[12] E. F. Drocella, Jr., et al., "3.5 GHz exclusion zone analyses and methodology", NTIA, Washington, DC, USA, Tech. Rep. 15-517, Jun. 2015.

[13] Locke, Gary, L. E. Strickling, and A. Secretary. "An assessment of the near-term viability of accommodating wireless broadband systems in the 1675-1710 mhz, 1755-1780 mhz, 3500-3650 mhz, and 4200-4220 mhz, 4380-4400 mhz bands", U. S. Dept. of Commerce, Washington, DC, October 1 (2010).

[14] FCC, GN Docket No. 12-354, "Reply Comments of Google Inc. On The Further Notice Of Rulemaking", August 15 2014.

[15] Skolnik, Merrill I. "Introduction to Radar", Radar Handbook 2 (1962).

[16] Nadav Levanon. "Radar Principles", 1st ed. USA: John Wiley and Sons, 1988.

[17] H. Ochiai, H. Imai. "On the distribution of the peak-to-average power ratio in ofdm signals" *Communications, IEEE Transactions on*, vol. 49, no. 2, pp. 282–289, Feb 2001.

[18] "NTIA letter to FCC on commercial operations in the 3550-3650 MHz band", NTIA, Washington, DC, USA, Tech. Rep. 12-354, GN 12-354, Apr. 2015.

[19] E. F. Drocella, L. Brunson, and C. T. Glass. "Description of a model to compute the aggregate interference from radio local area networks employing dynamic frequency selection to radars operating in the 5 ghz frequency range", NTIA, Tech. Rep., May 2009.

[20] M. Haenggi and R. K. Ganti. "Interference in large wireless networks", *Found. Trends Netw.*, vol. 3, no. 2, pp. 127–248, Feb. 2009.

[21] D. Stoyan, W. S. Kendall, and J. Mecke, "Stochastic Geometry and its Applications", John Wiley & Sons, second edition, 1995.

[22] Bianchi, Giuseppe. "Performance analysis of the IEEE 802.11 distributed coordination function." IEEE Journal on selected areas in communications 18.3 (2000): 535-547.

[23] Collins, Charles R., and Kenneth Stephenson. "A circle packing algorithm", Computational Geometry 25.3 (2003): 233-256.

[24] Longley, Anita G., and Patricia L. Rice. "Prediction of tropospheric radio transmission loss over irregular terrain. A computer method-1968". No. ITS-67. ITS Boulder CO, 1968.

[25] Public Wi-Fi Database using openBmap and OpenWifi. Available: https://www.mylnikov.org/archives/1170

[26] Snyder, John Parr. "Map projections–A working manual." Vol. 1395. US Government Printing Office, 1987.

[27] Diederik P. Kingma, Jimmy Ba, "Adam: A method for stochastic optimization", *International Conference on Learning Representations*, 1–13.

[28] M. Mehrnoush and S. Roy, "Spectrum Sensing and Interference Mitigation in Coexistence of WLAN Network with Radar", *IEEE Transactions on Cognitive Communications and Networking*, 2017.

[29] Huber, Peter J. "Robust estimation of a location parameter", The Annals of Mathematical Statistics 35.1 (1964): 73-101.

APPENDIX

Based on equations (2.24) and (3.6), optimal protection distance by limiting maximum outage probability is obtained as:

$$d_{opt} = \arg\min_{d(\theta)} \int_0^{2\pi} d^2(\theta) d\theta$$
$$\mu_I + \sigma_I Q^{-1}\left(P_{out,\max}\right) \leq I_{\max}$$

where μ_I and σ_I are calculated in (2.18) and (2.19):

$$\mu_I = C_{\mu_I} \int_\theta G(\theta) d^{2-\alpha}(\theta) d\theta$$
$$\sigma_I = \sqrt{C_{\sigma_I^2} \int_\theta G^2(\theta) d^{2-2\alpha}(\theta) d\theta}$$

Optimal $d(\theta)$ is attained by converting the inequality constraint to equality. This follows because for any $d(\theta)$ for which the strict inequality constraint holds, we can scale down $d(\theta)$ accordingly to increase μ_I, σ_I and achieve equality constraint (note that $2-\alpha < 0$ and $2-2\alpha < 0$). This will clearly result in a smaller objective function.

With equality constraint, we use Lagrange multiplier method with a dummy variable ϵ to redefine objective function as

$$d_{opt} = \arg\min_{d(\theta)} \int_0^{2\pi} d^2(\theta) d\theta + \epsilon \left(\mu_I + \sigma_I Q^{-1}\left(P_{out,\max}\right) - I_{\max}\right)$$

Taking partial derivatives of the new objective function with respect to $d(\theta)$ results in:

$$\frac{\partial f}{\partial d(\theta)} = 0, \qquad d(\theta) + \epsilon \left[\frac{\partial \mu_I}{\partial d(\theta)} + Q^{-1}(P_{out,\max}) \frac{\partial \sigma_I}{\partial d(\theta)}\right] = 0$$

Replacing μ_I and σ_I:

$$d(\theta) + \epsilon \left[(2-\alpha) C_{\mu_I} G(\theta) d^{1-\alpha}(\theta) + \frac{Q^{-1}(P_{out,\max}) C_{\sigma_I^2} (2-2\alpha) G^2(\theta) d^{1-2\alpha}(\theta)}{2\sqrt{C_{\sigma_I^2} \int_\theta G^2(\theta) d^{2-2\alpha}(\theta) d\theta}}\right] = 0$$

Appendix A

WHERE TO FIND THE FILES

All the code and documentation can be found on:

- FuNLAB webpage.

  `https://depts.washington.edu/funlab/research`

- My webpage

  `https://www.anishashok.com`

VITA

Anish Ashok is a Master of Science student in Electrical Engineering at the University of Washington.

His research focuses on wireless communications, computer networks and signal processing. At the university, he also works on a city-scale spectrum monitoring project: CityScape, that uses a web platform to control software defined radios and store I-Q data on a Cloud platform. Some of his publications are:

1. Hessar, F., Ashok, A. and Roy, S., "Radar Wi-Fi Spectrum Sharing - Evaluation of Radar protection regions," in *Radar & Communication Spectrum Sharing*, IET, London, 2017.

2. Roy, S., McHenry, M., Ashok, A., Kannam, S., Shin, K. S., Vigil, G. and Aragon, D., "CityScape: A Metro-area Spectrum Observatory," in *International Conference on Computer Communication and Networks (ICCCN)*, Vancouver, Canada, Aug 2017.

3. Ashok, A., Kumari, D., Satish, K., Eswar, S. and Chandar, T.S., "Robust control of UAVs using uncertainty and disturbance estimation," in *International Conference on Industrial Instrumentation and Control (ICIC)*, Pune, India, May 2015.

He welcomes your comments or queries to `anish1@uw.edu` or `anishashok.com`.